Monthly Notices of the ROYAL ASTRONOMICAL SOCIETY

MNRAS **475,** 2614–2631 (2018) doi:10.1093/mnras/sty009
Advance Access publication 2018 January 9

SNhunt151: an explosive event inside a dense cocoon

N. Elias-Rosa,[1,2★] S. Benetti,[1] E. Cappellaro,[1] A. Pastorello,[1] G. Terreran,[1] A. Morales-Garoffolo,[2] S. C. Howerton,[3] S. Valenti,[4] E. Kankare,[5] A. J. Drake,[6] S. G. Djorgovski,[6] L. Tomasella,[1] L. Tartaglia,[1,7] T. Kangas,[8] P. Ochner,[1] A. V. Filippenko,[9,10] F. Ciabattari,[11] S. Geier,[12,13] D. A. Howell,[14,15] J. Isern,[2] S. Leonini,[16] G. Pignata[17,18] and M. Turatto[1]

[1]*INAF – Osservatorio Astronomico di Padova, vicolo dell'Osservatorio 5, I-35122 Padova, Italy*
[2]*Department of Applied Physics, University of Cádiz, Campus of Puerto Real, E-11510 Cádiz, Spain*
[3]*1401 South A, Arkansas City, KS 67005, USA*
[4]*Department of Physics, University of California, Davis, CA 95616, USA*
[5]*Astrophysics Research Centre, School of Mathematics and Physics, Queen's University Belfast, Belfast BT7 1NN, UK*
[6]*Astronomy Department, California Institute of Technology, Pasadena, CA 91125, USA*
[7]*Department of Astronomy and Steward Observatory, University of Arizona, 933 N Cherry Ave, Tucson, AZ 85719, USA*
[8]*Tuorla Observatory, Department of Physics and Astronomy, University of Turku, Väisäläntie 20, FI-21500 Piikkiö, Finland*
[9]*Department of Astronomy, University of California, Berkeley, CA 94720-3411, USA*
[10]*Miller Senior Fellow, Miller Institute for Basic Research in Science, University of California, Berkeley, CA 94720, USA*
[11]*Osservatorio Astronomico di Monte Agliale, Via Cune Motrone, I-55023 Borgo a Mozzano, Lucca, Italy*
[12]*Gran Telescopio Canarias (GRANTECAN), Cuesta de San José s/n, E-38712 Breña Baja, La Palma, Spain*
[13]*Instituto de Astrofísica de Canarias, Vía Láctea s/n, E-38200 La Laguna, Tenerife, Spain*
[14]*Las Cumbres Observatory, 6740 Cortona Drive, Suite 102, Goleta, CA 93117, USA*
[15]*Department of Physics, University of California, Santa Barbara, Broida Hall, Mail Code 9530, Santa Barbara, CA 93106-9530, USA*
[16]*Osservatorio Astronomico Provinciale di Montarrenti, S.S. 73 Ponente, I-53018 Sovicille, Siena, Italy*
[17]*Departamento de Ciencias Físicas, Universidad Andres Bello, Avda. República 252, Santiago 8320000, Chile*
[18]*Millennium Institute of Astrophysics (MAS), Nuncio Monseñor Sótero Sanz 100, Providencia, Santiago, Chile*

Accepted 2017 December 21. Received 2017 December 21; in original form 2017 June 15

ABSTRACT

SNhunt151 was initially classified as a supernova (SN) impostor (nonterminal outburst of a massive star). It exhibited a slow increase in luminosity, lasting about 450 d, followed by a major brightening that reaches $M_V \approx -18$ mag. No source is detected to $M_V \gtrsim -13$ mag in archival images at the position of SNhunt151 before the slow rise. Low-to-mid-resolution optical spectra obtained during the pronounced brightening show very little evolution, being dominated at all times by multicomponent Balmer emission lines, a signature of interaction between the material ejected in the new outburst and the pre-existing circumstellar medium. We also analysed mid-infrared images from the *Spitzer Space Telescope*, detecting a source at the transient position in 2014 and 2015. Overall, SNhunt151 is spectroscopically a Type IIn SN, somewhat similar to SN 2009ip. However, there are also some differences, such as a slow pre-discovery rise, a relatively broad light-curve peak showing a longer rise time (∼50 d), and a slower decline, along with a negligible change in the temperature around the peak ($T \leq 10^4$ K). We suggest that SNhunt151 is the result of an outburst, or an SN explosion, within a dense circumstellar nebula, similar to those embedding some luminous blue variables like η Carinae and originating from past mass-loss events.

Key words: stars: evolution – supernovae: general – supernovae: individual: SNhunt151: galaxies: individual: UGC 3165.

1 INTRODUCTION

Massive stars can lose mass via steady winds, binary interaction, or as a consequence of dramatic eruptions, generating dense and structured circumstellar cocoons. When these stars explode as

★ E-mail: nancy.elias@oapd.inaf.it

supernovae (SNe), the ejecta interact with a pre-existing, optically thick circumstellar medium (CSM), producing collisionless shocks (see, e.g. Chevalier & Irwin 2012 or Ofek et al. 2013b) that convert the ejecta kinetic energy into radiation. This interaction strongly affects the SN spectroscopic and photometric display. The study of these observables gives us important clues to the progenitors' mass-loss rates, hence constraining the late evolution of massive stars (see, e.g. Smith 2014).

Early-time spectra of H-rich interacting SNe (Type IIn) are characterized by a blue continuum with narrow hydrogen emission lines, with full width at half-maximum (FWHM) velocities up to about 2000 km s^{-1}. These are believed to arise from the ionization of the pre-existing CSM because of its interaction with the SN ejecta. The narrow lines may have Lorentzian wings caused by electron scattering. However, relatively broad components (FWHM $\approx 10^4$ km s^{-1}) can also be produced by fast-moving SN ejecta and are detectable when the CSM is optically thin (see, e.g. Terreran et al. 2016). Interacting SNe display a large variety of spectral line components (having different widths and profiles) and photometric parameters (SNe with both slowly and rapidly declining light curves). These observational differences indicate a substantial diversity in the energetics, as well as in the configuration of the progenitor star and its environment at the moment of explosion.

The typical SN signatures can be masked at all phases if the SN ejecta interact with dense CSM. In particular, the elements produced during the explosive nucleosynthesis (including O, C, Mg) are not frequently detected in SNe IIn.

A growing number of interacting SNe preceded by major optical outbursts weeks to years before the SN explosion (Ofek et al. 2014) has been observed. These pre-SN outbursts are often called 'SN impostors' (e.g. SN 1997bs, Van Dyk et al. 2000; or the general discussions by Smith et al. 2011 and Van Dyk & Matheson 2012a) because they mimic in terms of energetic and spectral appearance a real SN explosion, though the star survives the burst. The discrimination between SN impostors and SNe IIn can be challenging. When outbursts of massive stars herald terminal SN explosions, the instabilities are presumably related to physical processes occurring when the star approaches the end of its evolution (see, e.g. Quataert & Shiode 2012; Smith & Arnett 2014; Fuller 2017). Well-studied examples include SN 2009ip (Smith et al. 2010; Foley et al. 2011; Fraser et al. 2013, 2015; Mauerhan et al. 2013; Pastorello et al. 2013a; Margutti et al. 2014; Graham et al. 2017), SN 2010mc (Ofek et al. 2013a; Smith, Mauerhan & Prieto 2014), LSQ13zm (Tartaglia et al. 2016), SN 2015bh (Elias-Rosa et al. 2016; Ofek et al. 2016; Thöne et al. 2017), and SN 2016bdu (Pastorello et al. 2017).

In this context, SNhunt151 (also known as PSN J04472985+2358555, XM07BW, and CSS131025: 044730+235856) is an interesting object. It was discovered by the Catalina Real-Time Transient Survey (CRTS; Drake et al. 2009)[1] on 2012 September 25.41 (UT dates are used hereafter) at $\alpha = 04^{\rm h}47^{\rm m}30\overset{\rm s}{.}00$, $\delta = +23^\circ 58' 56\overset{''}{.}0$ (J2000.0; Fig. 1). The object, hosted in the spiral galaxy UGC 3165, had an unfiltered magnitude of 20.7. The transient was re-observed, on 2013 August 30.17, showing a significant increase in its brightness, up to 17.6 mag.

The presence of an Hα emission line in the spectrum of 2013 September 02.21, showing a complex profile composed of broad and narrow components (Pastorello et al. 2013b, 2013c), is reminiscent of SN 2009ip. After the initial brightening, a further increase (by about 2 mag) in the luminosity was reported about 50 d later (Elias-Rosa et al. 2013).

In this manuscript, we present our study of SNhunt151. Basic information on the SN host galaxy, UGC 3165, is found in Section 2. Results of the photometric and spectroscopic monitoring campaign of SNhunt151 are presented in Sections 3 and 4. A discussion and brief summary follow in Section 5.

2 HOST GALAXY, DISTANCE, AND REDDENING

UGC 3165 is classified as an irregular galaxy (IAm[2]). From the average recession velocity of the galaxy corrected for Local Group infall into the Virgo cluster (Mould et al. 2000) $v_{\rm Vir} = 3783 \pm 3$ km s^{-1} ($z = 0.0126$), and assuming $H_0 = 73$ km s^{-1} Mpc^{-1}, we derive a distance of 51.8 ± 3.6 Mpc ($\mu = 33.57 \pm 0.15$ mag). This distance will be adopted throughout this paper.

The Milky Way extinction along the line of sight of the transient is quite large, $A_{V,\rm MW} = 1.88$ mag (NED; Schlafly & Finkbeiner 2011). Additionally, the higher resolution spectra of the transient (taken on 2013 September 2 and 2013 November 1; see Table B5) exhibit a blended Na I D feature at the recession velocity of the host galaxy, with an average equivalent width (EW) of 0.26 ± 0.02 Å. Using the relations given by Turatto, Benetti & Cappellaro (2003) and Poznanski, Prochaska & Bloom (2012), and assuming $R_V = 3.1$ (Cardelli, Clayton & Mathis 1989), we derive $A_{V,\rm host} \approx 0.09 \pm 0.02$ mag. Thus, we adopt $A_{V,\rm tot} = 1.97 \pm 0.19$ mag[3] ($E(B-V)_{\rm tot} = 0.64 \pm 0.06$ mag) as the total extinction towards SNhunt151. We caution that a large dispersion is observed in the EW (Na I D) versus $E(B-V)$ plane when a large SN sample is considered. For this reason, the derived extinction estimate cannot be considered secure (see, e.g. Elias-Rosa 2007; Poznanski et al. 2011; Phillips et al. 2013).

3 PHOTOMETRY

3.1 Ground-Based Observations

Optical *BVRI* (Johnson-Cousins system), *ugriz* (Sloan system), and near-infrared (NIR) *JHK* images of SNhunt151 were taken using a large number of observing facilities, listed in Table B1. After discovery, the transient was observed for about 14 months with a gap of ∼5 months when it was behind the Sun. Our data include 48 epochs taken before the discovery, starting on 2003 December [upper limit from the Sloan Digital Sky Survey (SDSS) DR9 [4]] up to 2012 March. These data were taken mainly by amateur astronomers. One epoch was secured using the Ultraviolet and Optical Telescope on board the *Swift* satellite on 2013 September 05.65. However, only upper limits were estimated for the *UVW2* (>20.9 mag) and *UVW1* (>20.0 mag) bands (VEGAMAG).

Photometric observations were preprocessed following the standard recipe in IRAF[5] for CCD images (trimming, overscan, bias, and flat-field corrections). For the NIR exposures, we also applied an

[1] http://crts.caltech.edu.

[2] NED, NASA/IPAC Extragalactic Database; http://nedwww.ipac.caltech.edu/.

[3] We consider a conservative uncertainty in the Milky Way extinction of about 10 per cent.

[4] http://www.sdss.org.

[5] IRAF is distributed by the National Optical Astronomy Observatory, which is operated by the Associated Universities for Research in Astronomy, Inc., under cooperative agreement with the National Science Foundation.

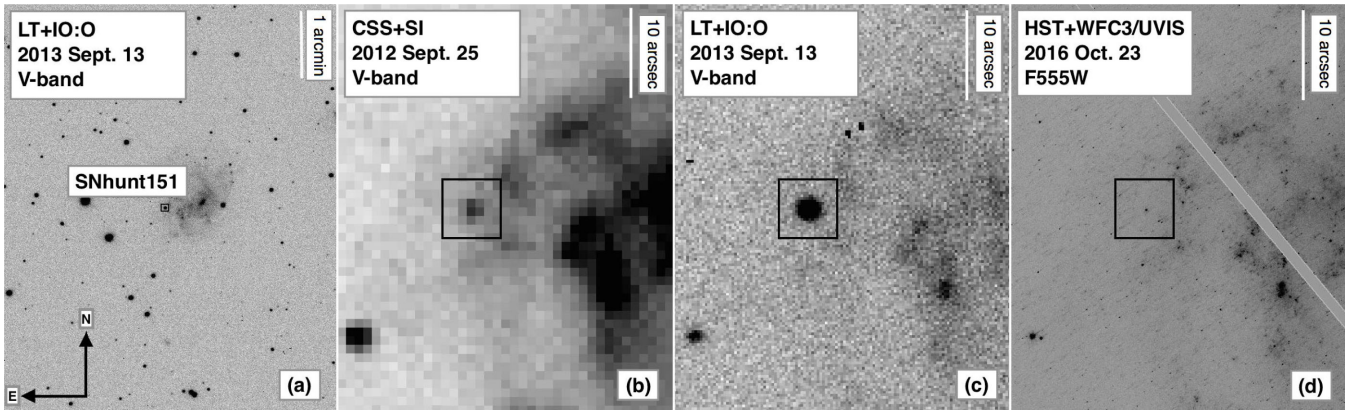

Figure 1. *V*- and *F*555*W*-band images of SNhunt151 in UGC 3165 obtained with the Liverpool Telescope+IO:O on 2013 September 13 (a,c), the Cassegrain reflector+SI on 2012 September 25 (b), and *HST*+WFC3/UVIS on 2016 October 23 (d). The location of the transient is indicated.

illumination correction and background-sky subtraction. For later epochs, multiple exposures obtained in the same night and filter were combined to improve the signal-to-noise ratio (S/N). The SN magnitudes were measured using point-spread-function (PSF) fitting with SNOoPy.[6] No template subtraction was performed since no major differences were found when comparing the photometry obtained through both PSF fitting and template subtraction. The data derived with the two methods are in agreement to within 0.1 mag.

In order to calibrate the instrumental magnitudes to standard photometric systems, we used the zero-points and colour terms measured through reference SDSS stars in the field of SNhunt151. The Johnson–Cousins magnitudes of these reference stars were calculated from the Sloan magnitudes following the conversions of Chonis & Gaskell (2008). For the NIR photometry, we used the Two Micron All Sky Survey (2MASS) catalogue as reference for the calibration. Once the local sequence was calibrated, we proceeded to calibrate our transient, even for non-photometric nights.

Unfiltered magnitudes from amateurs were scaled to Johnson–Cousins *V*- or *R*-band magnitudes, depending on the wavelength peak efficiency of the detectors. Uncertainty estimates were obtained through artificial-star experiments. This is combined (in quadrature) with the PSF fit error returned by DAOPHOT and the propagated errors from the photometric calibration.

The final calibrated SN magnitudes are listed in Tables B2 and B5 for the optical bands, and in Table B4 for the NIR range.

3.2 Space-Based Observations

The SNhunt151 site was also observed by the *Hubble Space Telescope* (*HST*) with the Ultraviolet-Visible (UVIS; $\sim$0.04 arcsec pixel^{-1}) Channel of the Wide-Field Camera 3 (WFC3) in the *F*555*W* and *F*814*W* bands. These images were taken on 2016 October 23 as part of the SN snapshot survey GO-14668 (PI: A. V. Filippenko), 1113.1 d after the *V*-band peak of SNhunt151's Event B (see below).

A source was detected at the transient position in all images with root-mean-square uncertainties <0.01 arcsec (Fig. 1d), through comparison with ground-based, post-discovery Copernico Telescope+AFOSC, and NOT+ALFOSC images taken on 2013 August 31 (seeing 1.16 arcsec) and 2014 August 24 (seeing 0.96 arcsec).

The magnitudes of the source in VEGAMAG were obtained using DOLPHOT.[7] We assume that the *F*555*W* and *F*814*W* bandpasses correspond approximately to Johnson–Cousins *V* and *I*, respectively; thus, we include these measurements in Table B2.

3.3 Light curves

The *ugri* and *BVRIJHK* light curves are shown in Fig. 2, relative to the *V* maximum date on 2013 October 06.3, or MJD 56571.8 (estimated by low-order polynomial fitting; in the following we will adopt this epoch as the reference). As we can see, SNhunt151 was discovered well before maximum light. The light curves also show a relatively fast decline after maximum, similar to those of the rapidly declining SNe II (e.g. Anderson et al. 2014). Optical light curves of SNhunt151 show post-maximum decline rates between 1.8 and 2.8 mag (100 d)$^{-1}$, and those in the NIR have a slightly slower decline ($\sim$1.8 mag (100 d)$^{-1}$). At late times (>300 d), SNhunt151 decreases in brightness by $\sim$5 mag with respect to maximum light, and shows a slower decline (<1.3 mag (100 d)$^{-1}$). Table 1 summarizes the magnitude and epochs at maximum light, as well as the decline rates of SNhunt151.

The SNhunt151 site was observed several times over almost a decade before the transient discovery (see Table B2 and Fig. 3, and Fig. 1b). Until the end of 2011, we did not detect a source at the position of the transient, at an absolute magnitude brighter than $-$13 mag. However, from December 2011, we began to detect some flux, followed by a slow luminosity rise (labelled Event A) of about 1.6 mag in 450 d ($\sim$0.2 mag (100 d)$^{-1}$), corresponding to a rise from $-$13.8 to $-$15 mag. Note that this rise may also consist of multiple distinct outbursts, since the observational campaign was interrupted twice. After August 2013, the transient brightness showed a much steeper increase, reaching a peak of $-$18.10 mag in *V* (labelled Event B), consistent with the typical magnitudes at peak of most Type IIn SNe (between $-$16 and $-$19 mag; Kiewe et al. 2012), or the Event B of the SN 2009ip-like family of transients ($M_{r/R} \lesssim -18$ mag; Pastorello et al. 2017, submitted).

[6] SNOoPy is a package for SN photometry developed by E. Cappellaro. A package description can be found at http://sngroup.oapd.inaf.it/snoopy.html.

[7] DOLPHOT is a stellar photometry package that was adapted from HSTPHOT for general use (Dolphin 2000) with the individual WFC3 pre-mosaic frames. We used the WFC3 module of v2.0, updated 2016 April; http://americano.dolphinsim.com/dolphot/.

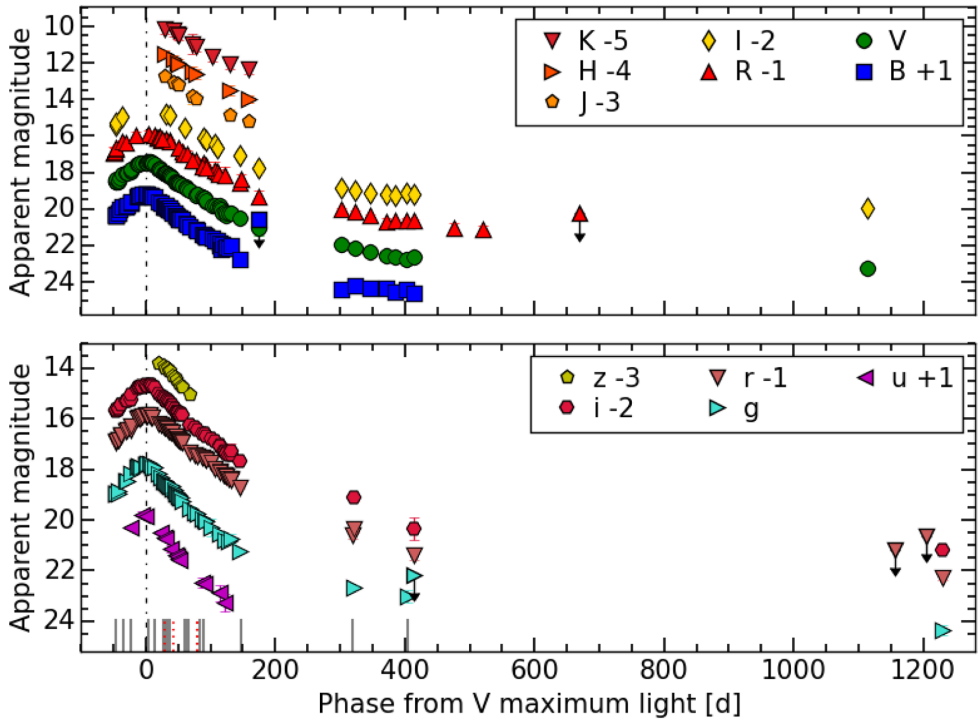

Figure 2. Optical and NIR light curves of SNhunt151. Upper limits are indicated by a symbol with an arrow. The solid and dotted marks on the abscissa indicate the phases at which optical and NIR spectra were obtained, respectively. The dot–dashed vertical line indicates the *V*-band maximum light of SNhunt151. The light curves have been shifted for clarity by the amounts indicated in the legend. The uncertainties for most data points are smaller than the plotted symbols. A colour version of this figure can be found in the online journal.

Table 1. Peak epochs, peak apparent magnitudes, and decline rates of SNhunt151 in different bands.

Band[a]	Early rise (Event A) [mag (100 d)$^{-1}$]	MJD_{max}	m_{max} (mag)	Decline from max[b] [mag (100 d)$^{-1}$]	Tail rate at $\gtrsim$ 300 d [mag (100 d)$^{-1}$]
B	–	56572.0 (0.8)	18.2 (0.1)	2.23 (0.26)	0.21 (0.15)
V	0.35 (0.15)	56571.8 (1.0)	17.4 (0.1)	2.09 (0.18)	0.69 (0.11)
R	0.35 (0.23)	56572.1 (1.2)	16.9 (0.1)	1.92 (0.24)	0.49 (0.15)
I	–	–	–	1.81 (0.17)	0.28 (0.08)
u	–	56568.3 (1.2)	18.8 (0.1)	2.39 (0.40)	–
g	–	56571.1 (0.4)	17.8 (0.1)	2.29 (0.18)	0.45 (0.23)[c]
r	–	56572.6 (0.8)	16.9 (0.1)	1.98 (0.16)	0.97 (0.19)
i	–	56571.9 (0.5)	16.7 (0.1)	2.04 (0.14)	1.32 (0.45)
z	–	–	–	2.81 (0.15)	–
J	–	–	–	1.85 (0.26)	–
H	–	–	–	1.80 (0.23)	–
K	–	–	–	1.84 (0.33)	–

Notes. [a]Apparent magnitude at peak of the *IzJHK* light curves could not be constrained.
[b]Considering the interval from ∼45 d to 175 d after *V*-band maximum light.
[c]Note that the tail rates for the Sloan bands were derived from just two epochs.

The *V* absolute magnitude light curve of SNhunt151 is compared in Fig. 3 with those of SN 2009ip (Maza et al. 2009; Smith et al. 2010; Foley et al. 2011; Fraser et al. 2013; Mauerhan et al. 2013; Pastorello et al. 2013a), SN 2015bh (Elias-Rosa et al. 2016), and the SN impostor SNhunt248 (Kankare et al. 2015). For these objects, we have adopted the distance and extinction values from the literature (see Table A1). From this comparison, we note that while the brightness at maximum of Event B of SNhunt151 is similar to those of the other transients in the sample (with the exception of the SN impostor SNhunt248 during its '2014b' peak), none of them matches the slowly rising Event A. We also note that the Event B light curve of SNhunt151 is broader than those of the other transients, with both a longer rise time and a slower decline.

We also find differences in the colour curves of the objects of our sample (Fig. 4). SNhunt151 shows a relatively flat and slow colour evolution towards the red for the $(B - V)_0$ and $(V - R)_0$ colours, but an almost constant $(R - I)_0$ colour. The approximated Johnson–Cousins colour at our last epoch (phase 1229 d, adopting the conversions of Chonis & Gaskell 2008) also follows this trend. No other object from our sample of comparisons exhibits similar behaviour.

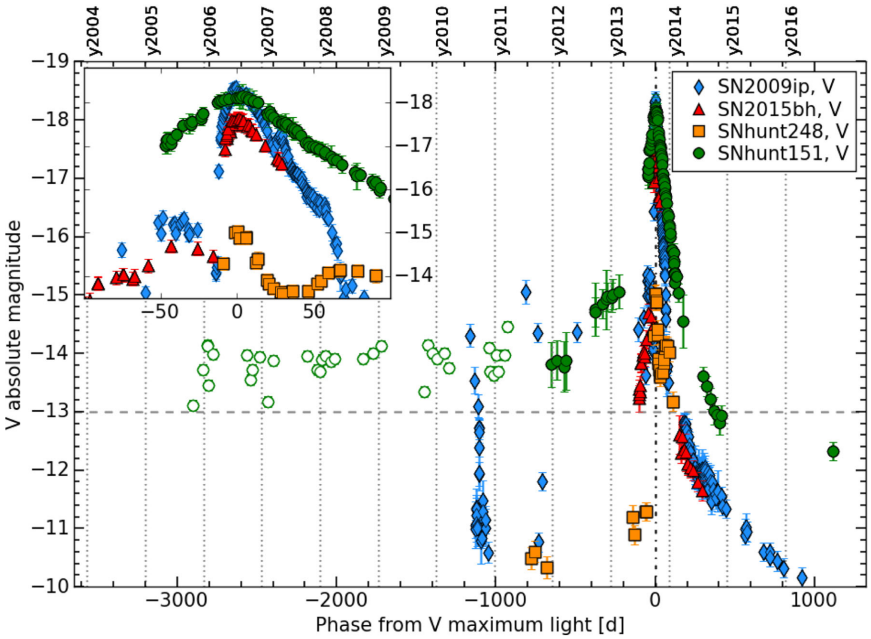

Figure 3. Historical absolute *V* light curve of SNhunt151, shown along with those of SN 2009ip, SN 2015bh, and SNhunt248. Upper limits for SNhunt151 are indicated by empty circles with arrows. The dashed horizontal line indicates the boundary of −13 mag, whereas the dot–dashed vertical line indicates the *V*-band maximum light of SNhunt151. Note that the first epoch of SNhunt151 is an approximation from Sloan magnitudes. A colour version of this figure can be found in the online journal.

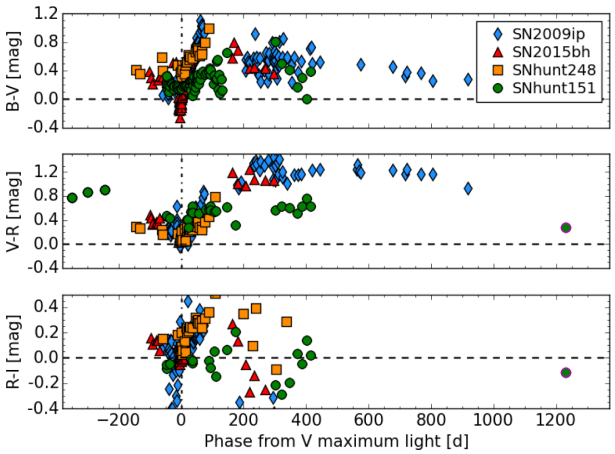

Figure 4. Intrinsic colour curves of SNhunt151, compared with those of SN 2009ip, SN 2015bh, and SNhunt248. The dot–dashed vertical line indicates the *V*-band maximum light of SNhunt151. Note that the last epoch of SNhunt151 is an approximation from Sloan magnitudes. A colour version of this figure can be found in the online journal.

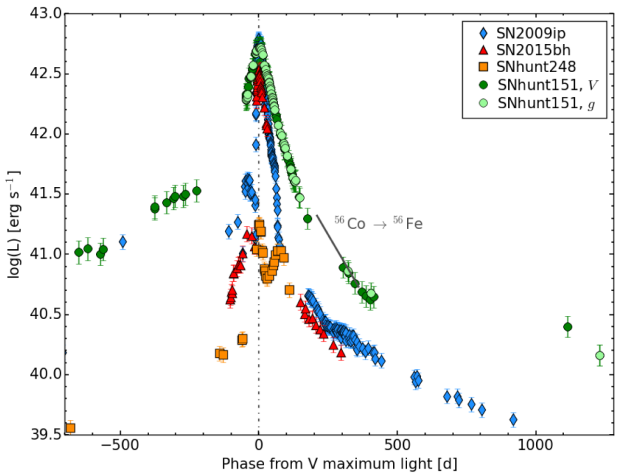

Figure 5. Pseudobolometric light curve of SNhunt151 obtained by integrating optical and NIR bands at epochs where *V* or *g* were available, compared with those of SN 2009ip, SN 2015bh, and SNhunt248. The dot–dashed vertical line indicates the *V*-band maximum light of SNhunt151. A colour version of this figure can be found in the online journal.

We computed a pseudobolometric light curve of SNhunt151, integrating the wavelength range covered from the *u* to the *K* bands (Fig. 5). The fluxes at the effective wavelengths were derived from extinction-corrected apparent magnitudes, when observations in the *V* or *g* bands were available. When no observation in individual filters was available, the missing photometric epoch was recovered by interpolating the values from epochs close in time or, when necessary, extrapolating assuming a constant colour from the closest available epoch. The pseudobolometric fluxes were estimated integrating the spectral energy distribution (SED) at each epoch following the trapezoidal rule, and assuming zero contribution outside the integration boundaries. Finally, the luminosity was derived from the integrated flux accounting for the adopted distance. The bolometric luminosity errors account for the uncertainties in the distance estimate, the extinction, and the apparent magnitudes. The pseudobolometric light curves of SN 2009ip, SN 2015bh, and SNhunt248 were computed in a similar manner as that of SNhunt151.

Fitting low-order polynomials to the pseudobolometric light curve of SNhunt151, we estimate a peak luminosity for Event B of $(5.2 \pm 1.3) \times 10^{42}$ erg s^{-1}. The pseudobolometric peak of SNhunt151 is comparable to that of SN 2009ip, and is more

Table 2. Pseudobolometric maximum luminosities.

Object	Luminosity (10^{42} erg s^{-1})
SN 2009ip	6.1 (1.3)
SN 2015bh	3.3 (0.7)
SNhunt248	0.2 (0.1)
SNhunt151	5.2 (1.3)

luminous than those of the other transients of the sample (see Fig. 5 and Table 2). Note that the Event A maximum is around 15 times fainter than the light-curve peak of Event B. The pseudobolometric tail of SNhunt151 seems to follow roughly the radioactive decay tail of ^{56}Co to ^{56}Fe seen in SNe II, at least until ∼400 d. However, the last two points taken at phase >1100 d are brighter by ∼6 mag than the expected luminosity of a ^{56}Co-decay-powered light curve.

4 SPECTROSCOPY

Spectroscopic monitoring of SNhunt151 started soon after the confirmation of the object, on 2013 August 20, and lasted 15 months. We collected a total of 16 optical and 4 NIR spectra. Basic information on the spectroscopic observations can be found in Table B5.

All spectra were reduced following standard procedures with IRAF routines. The two-dimensional frames were debiased and flat-field corrected, before the extraction of the one-dimensional spectra.

Several pairs of NIR spectra were taken at each epoch at different positions along the slit, and consecutive pairs were subtracted from each other in order to remove the sky background. The subtracted images were aligned to match the spectrum profile and added together. Finally, the source spectrum was extracted from the combined images.

The one-dimensional optical and NIR spectra were then wavelength calibrated by comparison with arc-lamp spectra obtained during the same night and with the same instrumental configuration, and flux calibrated using spectrophotometric standard stars. The wavelength calibration was verified against the bright night-sky emission lines and adjusted if necessary. The absolute flux calibration of the spectra was cross-checked against the broad-band photometry and corrected, when necessary. Finally, the strongest telluric absorption bands in the optical spectra were removed using standard-star spectra (in some cases, residuals are still present after the correction).

4.1 Spectral evolution

Fig. 6 shows the sequence of optical and NIR spectra of SNhunt151, whereas in Fig. 7, we compare the optical spectra at representative epochs with those of the Type IIn SN 1996al (Benetti et al. 2016), and the transients SN 2009ip (Fraser et al. 2013, 2015; Pastorello et al. 2013a), SN 2015bh (Elias-Rosa et al. 2016), and SNhunt248[8] (Kankare et al. 2015) at similar epochs. All of the spectra have been corrected for extinction and redshift using values from the literature (see also Table A1).

[8] Note that the SNhunt248 phases are considered with respect to its major peak, "2014b."

The spectra of SNhunt151 taken from ∼− 47 d to 89 d during Event B exhibit a rather blue continuum and very little evolution. They are dominated by multicomponent Balmer lines in emission, and some relatively weak Fe II features. Although the Balmer lines do not show evolution during this period, the iron lines become slightly stronger after 65 d from maximum light. We can also distinguish two broad emission features centred at 6130 and 7200 Å (they are more evident in the spectra between phases 59 and 82 d), with FWHM ≈100 and 175 Å (∼4700 and 8000 km s^{-1}), respectively. Similar structure is not seen in Hβ. A possible explanation is the presence of a bipolar jet interacting with the dense CSM. This mechanism was also proposed for SN 2010jp, which shows a roughly similar (but rapidly evolving) Hα profile (Smith et al. 2012).

The photospheric temperatures at these epochs are estimated by fitting the SED of SNhunt151 with a blackbody function after removing the strongest features of the spectra. As shown in Fig. 8(a) and in Table 3, there is no clear evidence of variation of temperature around the peak. This is in the range 8300–9900 K (a lower temperature was estimated only for the last spectrum taken just before the seasonal gap, 89 d after maximum light). This behaviour is not seen in other Type IIn SNe (e.g. Taddia et al. 2013), or for the reference transients used here. In all these cases, the temperature is close to 20 000 K at the major peak, decreasing later to 8000–5000 K, and then remaining nearly constant in the following days; see, for example, SN 2009ip (Margutti et al. 2014) and SN 2015bh (Elias-Rosa et al. 2016). We also estimated and plotted the photospheric temperatures derived from the SED of SNhunt151 obtained from broad-band photometry. Here, there is some evidence of evolution, with a possible slow decrease of temperature after Event B. Similarly, the radius of the photosphere exhibits a likely slow evolution peaking at 11.6×10^{14} cm during Event B, and then decreases to 1.8×10^{14} cm at 146 d (Fig. 8b). At later phases (60 and 80 d after the peak of Event B), the estimated radius seems to increase and then decrease again. This fluctuation of the value of the photospheric radius is possibly caused by a geometric effect (e.g. an asymmetry in the CSM distribution) or a non-linear CSM density profile (see, e.g. Benetti et al. 2016). Note that these estimates of the radius are approximate, owing to the assumptions made to derive the temperatures and the luminosities of SNhunt151. For instance, the derived temperatures are more likely lower limit estimates since we have assumed blackbody spectra without taking into account effects such as the metal line blanketing.

Around maximum light, SNhunt151 spectra are dominated by Balmer features such as those of the transients SN 2009ip and SN 2015bh. SNhunt151, unlike these transients, does not show He I features, and its Hα profile exhibits a broader component (Fig. 7a). At phase 65–68 d (Fig. 7b), SNhunt151 is still relatively blue, whereas the other transients at the same phase turned red. Another difference to be noted is the absence of P-Cygni minima in the iron and Balmer lines.

At late phases (>145 d), the broader component of the Hα line seems to be weakening, whereas the spectra are still dominated by the narrow component (see Section 4.2). Resolved narrow lines (∼900 km s^{-1} FWHM) of He I λ5876, λ6678, and λ7065 are now evident in the spectra, as well as [Ca II] λλ7291, 7323. A hint of O I λ7774 might be identified, but because of the low S/N in that region, it is only a tentative identification. Fe II lines are still strong and show low-contrast P-Cygni profiles (for example, Fe II λ4923, λ5018, and λ5169) with expansion velocities between 900 and 1400 km s^{-1} from the absorption minima.

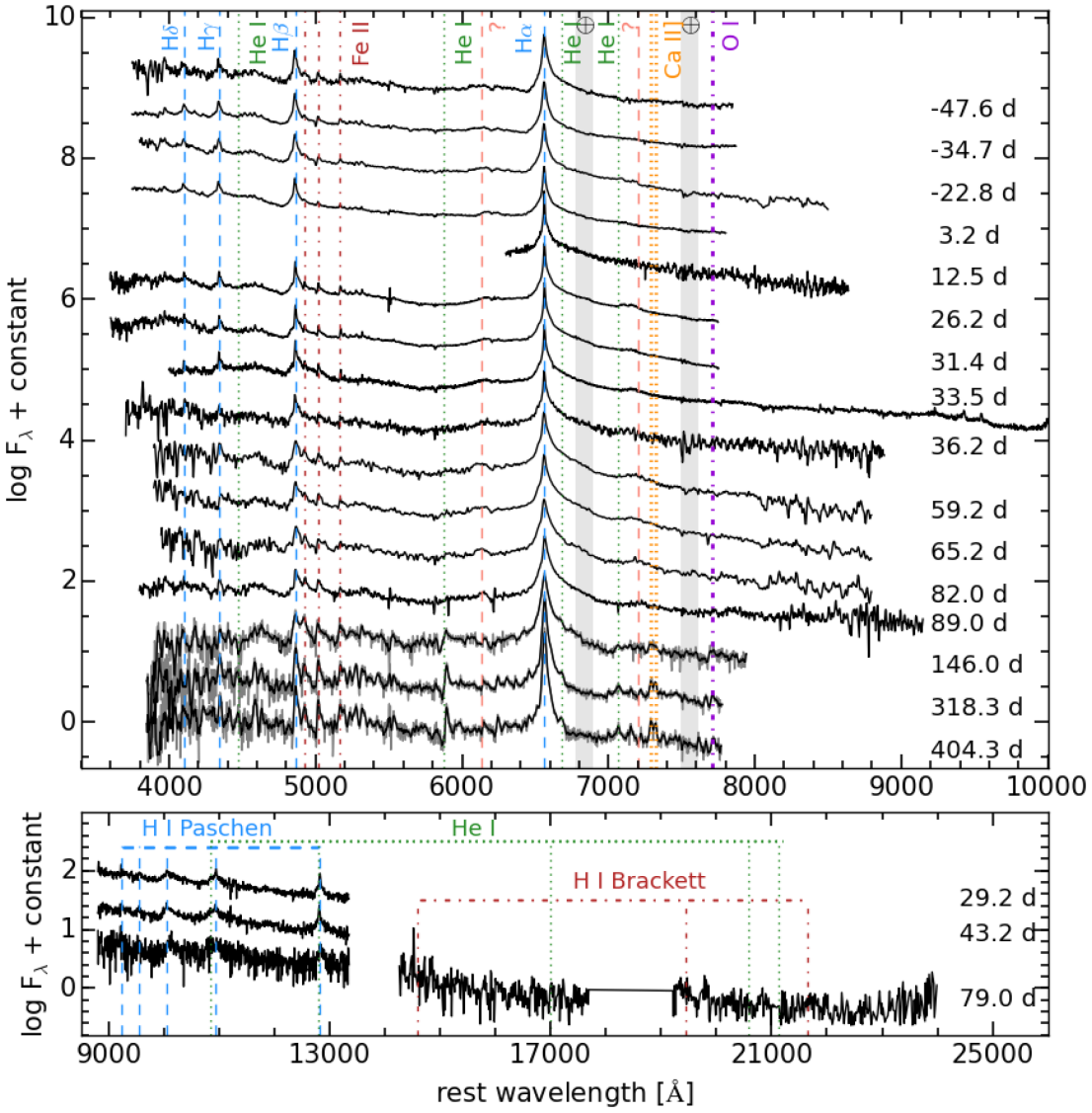

Figure 6. Sequence of optical and NIR spectra of SNhunt151 taken from 2013 August 20 to 2014 November 14. The late-time spectra at 146.0, 318.3, and 404.3 d are shown in grey, with a boxcar-smoothed (using an 8-pixel window) version of the spectra overplotted in black. All spectra have been redshift and extinction corrected. The locations of the most prominent spectral features are indicated by vertical lines. A colour version of this figure can be found in the online journal.

These features are still weak if we compare SNhunt151 spectra with those of the transients of our sample at similar epochs (Fig. 7c). We also highlight the differences between the Hα profiles (see inset in Fig. 7c), and SNhunt151, showing a quite symmetric profile. This is similar to that of SN 2009ip, except for an extended red wing of SNhunt151, and unlike the asymmetric Hα profiles of SNhunt248 and SN 2015bh, or the double-peaked one of SN 1996al.

The NIR spectra of SNhunt151 (Fig. 6, lower panel) are dominated by the hydrogen Paschen series. A trace of Brγ and He I features may also be detected. In fact, comparing the profile of the strongest Paschen lines of our spectrum at phase ~30 d with Hα at a similar epoch (Fig. 9e), we can see how the Paschen line at λ10940 is clearly blended with He I λ10 830, whereas the line at 12 820 Å is similar to Hα but apparently without the broad red wing. As at optical wavelengths, no P-Cygni profiles are seen.

4.2 Evolution of the Balmer lines

Hα is the most prominent line in the SNhunt151 spectra, and the analysis of its profile may allow us to probe the environment of the transient. As we can see in Fig. 9, the Hα profile seems to consist of multiple components that do not show relative evolution with time. Hβ exhibits a similar profile at earlier phases, but it is probably contaminated by iron lines at phases later than ~50 d. Following a procedure described by Elias-Rosa et al. (2016) for SN 2015bh, we decompose the line profile at all epochs into three emission components. We used a Lorentzian profile for the narrow component, and Gaussian functions for the intermediate and broad components, except for the two latest-time spectra in which there is no evidence for a broad component. Fig. 10 displays the results of the multicomponent fit at some representative epochs: 3.2, 65, 146, and 318 d. The derived velocities are listed in Table 3, and their evolution is shown in Fig. 8c.

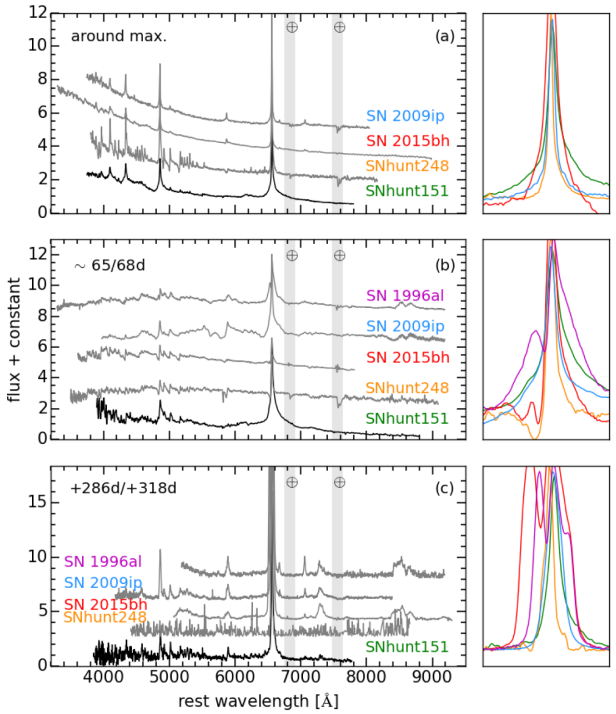

Figure 7. Comparison of SNhunt151 spectra around (a) the maximum of the major peak, and (b) 65–68 d and (c) 146–193 d after the peak, with those of the transients SNe 1996al, 2009ip, 2015bh, and SNhunt248 at similar epochs. The H α profiles are enlarged in the right-hand side of each panel, and normalized to the peak. All spectra have been corrected for their host-galaxy recession velocities and for extinction (values adopted from the literature). A colour version of this figure can be found in the online journal.

The FWHM of the narrow H α emission[9] remains nearly constant, with a velocity of $\sim$500 km s^{-1} as determined from our highest resolution spectra ($\sim$150–215 km s^{-1}). The intermediate component, related to the shocked ejecta region between the forward shock and the reverse shock, also remains roughly constant with an average FWHM of $\sim$3600 km s^{-1}. The broader component also exhibits an apparently constant evolution ($\sim$14 000 km s^{-1} FWHM), and then disappears in the last two spectra (>318 d).

The velocity of the broad component of H α is high in comparison with the velocities of the H-rich material expelled in major eruptions of massive stars such as luminous blue variables (LBVs; e.g. Smith 2008; Pastorello et al. 2013a). It is more indicative of an SN explosion, but in this case, the lack of evolution is rather puzzling. In fact, it is likely possible that the broad component is the Lorentzian wing of the narrow line, owing to electron scattering in the opaque CSM (e.g. Chugai 2001).

Interestingly, the total luminosity of the H α line (Fig. 8d, and Table 3) remains almost constant at $\sim 80 \times 10^{39}$ erg s^{-1} until $\sim$50 d, and decreases thereafter to $\sim 3 \times 10^{39}$ erg s^{-1} in our last spectrum.

5 DISCUSSION AND SUMMARY

In the previous sections, we analysed the observed properties of SNhunt151. This transient shows a slow rise of around 450 d, ranging from a *V*-band absolute magnitude of approximately -13.8 mag

[9] The narrow-line component was resolved in all spectra. We first corrected the measured FWHM for the spectral resolution, and then computed the velocity.

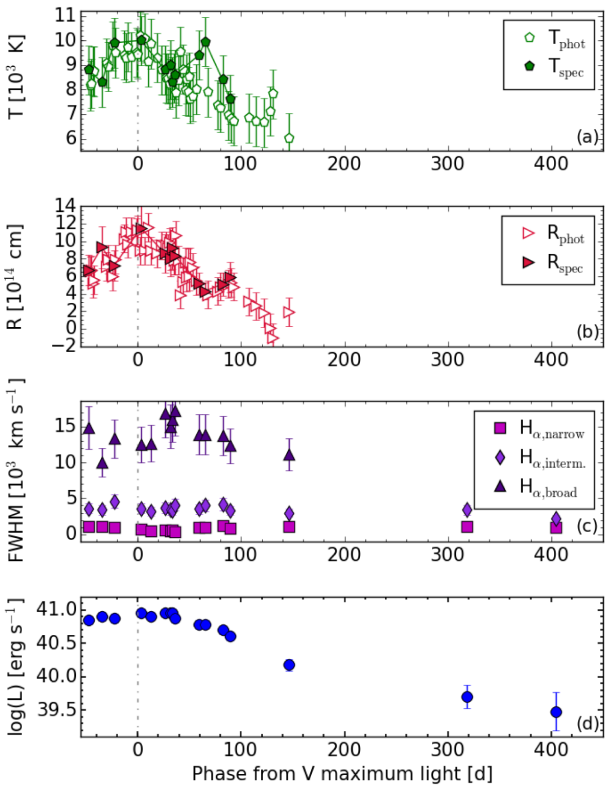

Figure 8. (a): evolution of the best-fitting blackbody temperatures; (b): evolution of the radius of the photosphere. The solid line connects the temperature and radius measurements; (c): FWHM evolution for the broad and narrow H α emission; (d): evolution of the total luminosity of H α. The dot–dashed vertical line indicates the *V*-band maximum light of SNhunt151. A conservative uncertainty of about $\pm$1000 K for the temperature has been assumed.

to -15.0 mag, then followed by a major re-brightening that peaks at -18.1 mag. Recent *HST*+WFC3 and GTC+OSIRIS images, taken around 3 yr after maximum, show a source at the position of SNhunt151 of $\sim-$ 12 mag in *F555W* ($\sim$*V*) and -11.6 mag in *g*. These late epochs do not follow the typical radioactive heating expected in SNe II, but instead indicate a shallower decline. During Event B, the spectra are always dominated by Balmer lines, and show negligible evolution.

As for other similar transients found in the last decade (e.g. SN 2009ip), it is arduous finding a unique interpretation for the chain of events of SNhunt151. As seen in previous sections, some observables of SNhunt151 could resemble those of the SN 2009ip-like transients. However, there are also significant differences, as follows.

(1) No significant variability brighter than -13 mag in the historical light curve (from the end of 2003 to the end of 2011).
(2) Slow prediscovery rise (Event A).
(3) Broad Event B with respect to other SN 2009ip-like transients.
(4) Stronger ejecta–CSM interaction (or a thicker envelope) over its entire evolution.
(5) No clear evidence of evolution in the temperature.
(6) No evidence of P-Cygni profiles in the Balmer lines during the entire evolution, and in iron features until phase $\sim$90 d.

A possible scenario is that during the outbursts, SNhunt151 is surrounded by a nebula or cocoon of material hiding the inner engine.

Table 3. Main parameters as inferred from the spectra of SNhunt151. The velocities are computed from the decomposition of the H α profile.

Date	MJD	Phase (days)	Temperature[a] (K)	FWHM$^{b}_{H\alpha,nar}$ (km s^{-1})	FWHM$_{H\alpha,\,inter}$ (km s^{-1})	FWHM$_{H\alpha,\,br}$ (km s^{-1})	Luminosity$_{H\alpha}$ (10^{39} erg s^{-1})	EW$_{H\alpha}$[c] Å
20130820	56524.20	−47.6	8800	1020 (204)	3600 (720)	14 860 (2972)	70 (10)	300 (60)
20130902	56537.18	−34.7	8300	1070 (214)	3400 (680)	10 000 (2000)	80 (12)	240 (50)
20130914	56549.01	−22.8	9900	970 (194)	4600 (920)	13 300 (2660)	75 (11)	195 (40)
20131010	56575.07	3.2	8600	650 (130)	3600 (720)	12 500 (2500)	90 (13)	190 (40)
20131019	56584.31	12.5	–	430 (86)	3150 (630)	12 650 (2530)	80 (11)	200 (40)
20131102	56598.05	26.2	8800	580 (116)	3700 (740)	16 800 (3360)	90 (12)	200 (40)
20131107	56603.26	31.4	9000	450 (90)	3400 (680)	15 000 (3000)	90 (12)	220 (45)
20131109	56605.39	33.5	8300	570 (114)	3300 (660)	16 000 (3200)	90 (13)	230 (45)
20131112	56608.04	36.2	8600	390 (78)	4100 (820)	17 200 (3440)	75 (11)	260 (50)
20131205	56631.07	59.2	9400	910 (182)	3500 (700)	13 900 (2780)	60 (9)	270 (50)
20131211	56637.00	65.2	9950	980 (196)	4000 (800)	13 900 (2780)	60 (9)	290 (60)
20131227	56653.85	82.0	8400	1220 (244)	4200 (840)	13 700 (2740)	50 (7)	280 (55)
20140103	56660.87	89.0	7600	840 (168)	3300 (660)	12 300 (2460)	40 (6)	270 (55)
20140301	56717.88	146.0	–	1070 (214)	3000 (600)	11 100 (2220)	15 (3)	285 (55)
20140821	56890.19	318.3	–	1020 (204)	3400 (680)	–	5 (2)	280 (55)
20141115	56976.16	404.3	–	900 (180)	2200 (440)	–	3 (2)	300 (60)

Notes. [a]We consider a conservative uncertainty in the temperature of about ±1000 K.
[b]We consider a conservative uncertainty in the velocities of about 20 per cent.
[c]We consider a conservative uncertainty in the EW of about 20 per cent.

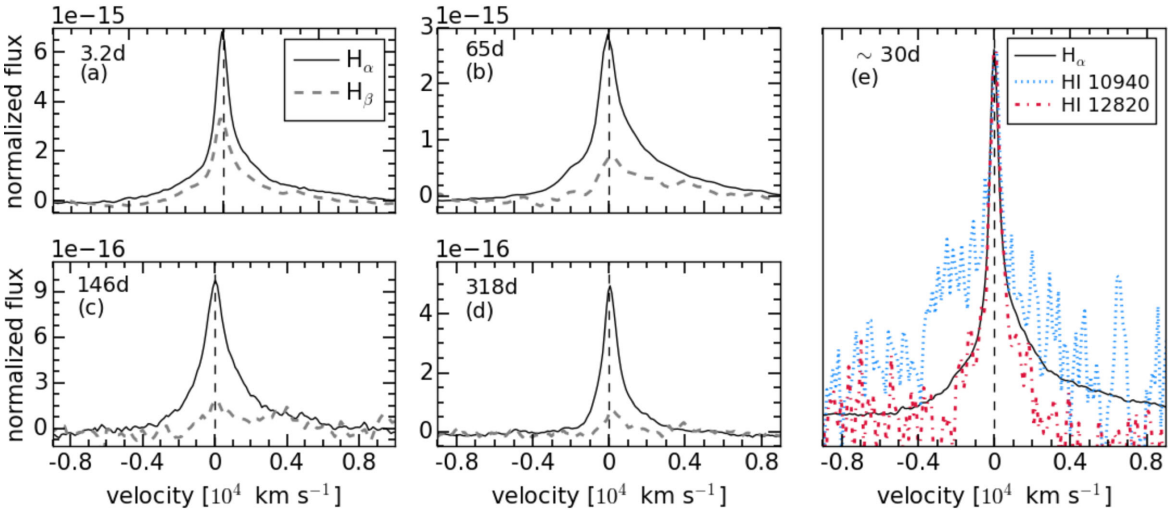

Figure 9. (a–d): H α and H β line profiles at representative epochs. (e): H α and Paschen λ10 940 and λ12 820 lines at phase ∼30 d, normalized to the peak. The dashed lines mark the rest wavelength of H α.

In some respects, this resembles the case of the Homunculus Nebula around η Carinae (e.g. Smith 2012). The nebula would enclose a recent event that can be almost anything, such as a collision between massive shells ejected by a very massive star, a merger event in a close binary system, or a terminal core-collapse SN explosion (either during Event A with the successive strong interaction of the SN ejecta and a circumstellar shell, or during Event B preceded by a giant eruption in Event A). One of the possible explanations for the lack of spectral evolution is that we are observing an asymmetric environment from an unfavourable orientation, where the more dense material conceals what is below.

Using the pseudobolometric luminosity, we attempt to constrain the total energy radiated by SNhunt151. We estimate an energy of 7.4×10^{48} erg during Event A, and 4.2×10^{49} erg during Event B. The latter radiated energy is comparable to that of SNe IIn such as SN 2011ht (∼3×10^{49} erg; Roming et al. 2012), or even the luminous SN 1998S (∼9×10^{49} erg; Fassia et al. 2000; Liu et al. 2000; Pozzo et al. 2004). These values are also similar to the high energy of other types of transients, such as the controversial SN 2009ip (∼1.5×10^{48} erg and ∼3×10^{49} erg for its respective events 2012a and 2012b; Margutti et al. 2014), or SN 1961V (∼4×10^{48} erg during the prepeak plateau, and ∼6×10^{49} erg during the major and brief peak; Bertola 1963, 1964, 1965, 1967). The 'Great Eruption of η Carinae released a radiated energy of ∼5×10^{49} erg (e.g. Humphreys & Martin 2012); however, it is noteworthy that the eruption lasted 20 yr. Summarizing, the amount of energy radiated during both Event A and Event B of SNhunt151 is not a conclusive argument to assess whether the object is a terminal event.

The main puzzle is Event A. Slow rising light curves have been previously seen in some Type IIn SNe, such as SN 2008iy (Miller et al. 2010), but with a luminosity at the peak which is a factor of 2.5 brighter than the maximum luminosity of SNhunt151 Event A. Given the SNhunt151 observables, it seems unavoidable that there is a considerable amount of opaque material between the engine and

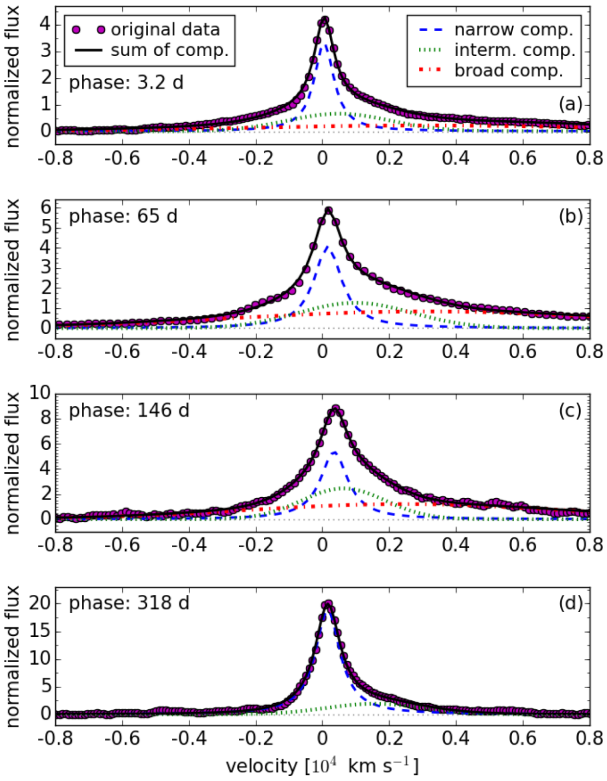

Figure 10. Decomposition of the Hα emission line of SNhunt151 at 3.2, 65, 146, and 318 d from *V*-band maximum light. A colour version of this figure can be found in the online journal.

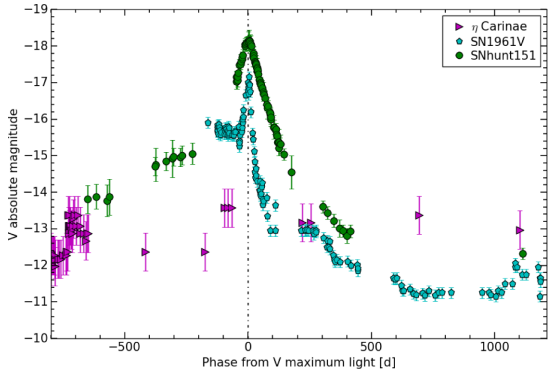

Figure 11. Absolute *V*-light curve of SNhunt151 (circles), shown along with those of supernova (or impostor) SN 1961V (pentagons; photographic mag) and the revised visual light curve of the Great Eruption of η Carinae (rotated triangles). The dot–dashed vertical line indicates the *V*-band maximum light of SNhunt151. A colour version of this figure can be found in the online journal.

the observer. Thus, the diffusion of the photons through the material is slow. Following the relations reported by Ofek et al. 2013a, from the rise time of the possible SN explosion (i.e. from Event B of SNhunt151, ∼50 d), we can estimate an upper limit to the amount of mass between the transient and us. Assuming as wind velocity the value inferred for the narrow Hα component during that rise (∼1000 km s^{-1}), we derive a mass-loss rate <1.1 M$_\odot$ yr^{-1}. This value is comparable to that of LBV giant eruptions (e.g. Smith 2016).

One interesting comparison is with SN 1961V. As we see in Fig. 11, the magnitude at the end of Event A of SNhunt151 is suggestively similar to that of the pseudoplateau shown by SN 1961V before its peak. The origin of this first event in SN 1961V depends on the interpretation. If SN 1961V was a true core-collapse SN (Smith et al. 2011; Kochanek, Szczygiel & Stanek 2011), then the light curve could be a combination of a Type II-Plateau-like SN, followed by a peak arising from interaction of the SN ejecta with the CSM. Instead, if the SN 1961V is a SN impostor (e.g. Van Dyk & Matheson 2012a,b), the pre-peak event is due to a series of minor eruptions and interaction with the material previously ejected.

An argument against the interpretation of SN 1961V as an SN impostor is the lack of detectable mid-infrared (MIR) emission at the transient position, expected from the dust shell formed around surviving LBVs (Kochanek et al. 2011). A counterexample is η Carinae, which is extremely luminous at IR wavelengths (e.g. Smith 2012).

Looking for some evidence of dust around SNhunt151, we inspected the *Spitzer Space Telescope* Heritage Archive[10] after the transient discovery. We found images at four epochs: 2005 February 23 and 24 (3.6, 4.5, 5.8, and 8.0 μm channels; Programme ID 3584, PI D. Padgett), 2014 November 27 (3.6 and 4.5 μm channels; Programme ID 10139, PI O. D. Fox), and 2015 May 23 (3.6 and 4.5 μm channels; Programme ID 11053, PI O. D. Fox), taken with the InfraRed Array Camera (IRAC) aboard *Spitzer*. We worked with the *Post Basic Calibrated Data (pbcd)*, which are already fully co-added and calibrated. We did not detect a source at the SNhunt151 position in the first two epochs (year 2005); however, a source is well detected in the last two (years 2014 and 2015) in both *Spitzer* channels. We estimate the integrated flux of the source (in the observations of 2005 we use an aperture of 3 × 3 pixels around the transient position) using MOPEX.[11] Following the 'recipe' advised by the *Spitzer* team, we obtained the values reported in Table 4 . The late-time NIR detections may suggest the formation of dust in a cool dense shell in SNhunt151, as in η Carinae and other SNe IIn (e.g. Fox et al. 2011, 2013) or, alternatively, an IR echo produced by foreground, pre-existing dust.

In summary, here we have discussed our observations of a unique object, SNhunt151. Its nature is still uncertain, but we support the hypothesis that we are observing a dense nebula of material and dust at the position of the transient, which reprocesses radiation from the underlying energetic outburst and enshrouds the mechanism that gives rise to the chain of events. It is clear that we should still keep an eye on SNhunt151 in the future.

ACKNOWLEDGEMENTS

We thank S. Spiro, R. Rekola, A. Harutyunyan, and M. L. Graham for their help with the observations. We are grateful to the collaboration of Massimo Conti, Giacomo Guerrini, Paolo Rosi, and Luz Marina Tinjaca Ramirez from the Osservatorio Astronomico Provinciale di Montarrenti. The staffs at the different observatories provided excellent assistance with the observations.

The research leading to these results has received funding from the European Union Seventh Framework Programme (FP7/2007-2013) under grant agreement No. 267251, 'Astronomy Fellowships in Italy' (AstroFIt)'. NE-R acknowledges financial support from MIUR PRIN 2010-2011, 'The Dark Universe and the Cosmic Evolution of Baryons: From Current Surveys to Euclid'. NE-R, AP,

[10] http://sha.ipac.caltech.edu/applications/Spitzer/SHA/.

[11] mopexis a *Spitzer* software package: http://irsa.ipac.caltech.edu/data/SPITZER/docs/dataanalysistools/tools/mopex/.

Table 4. *Spitzer* integrated fluxes of the SNhunt151 field.

Date	MJD	Phase[a] (days)	3.6 μm (μJy)	4.5 μm (μJy)	5.8 μm (μJy)	8.0 μm (μJy)	Program ID/P.I.
20050223	53424.87	−3147.0	<49.8	<29.0	<567.8	<1290.0	3584/D. Padgett
20050224	53425.39	−3146.5	<63.4	<46.0	<699.6	<1298.0	3584/D. Padgett
20141127	56988.00	416.2	14.5(0.2)	20.7(0.3)	–	–	10139/O. D. Fox
20150523	57165.81	594.0	12.6(0.4)	14.6(0.3)	–	–	11053/O. D. Fox

[a]Phases are relative to *V* maximum light, MJD =56571.8 ± 1.0.

SB, LT, MT, and GP are partially supported by the PRIN-INAF 2014 (project 'Transient Universe: Unveiling New Types of Stellar Explosions with PESSTO'). GP acknowledges support provided by the Millennium Institute of Astrophysics (MAS) through grant IC120009 of the Programa Iniciativa Científica Milenio del Ministerio de Economía, Fomento y Turismo de Chile. TK acknowledges financial support from the Emil Aaltonen Foundation. CRTS was supported by the NSF grants AST-0909182, AST-1313422, and AST-1413600. AVF is grateful for generous financial assistance from the Christopher R. Redlich Fund, the TABASGO Foundation, the Miller Institute for Basic Research in Science (UC Berkeley), and NASA/HST grant GO-14668 from the Space Telescope Science Institute, which is operated by AURA, Inc. under NASA contract NAS5-26555. The work of AVF was conducted in part at the Aspen Center for Physics, which is supported by NSF grantPHY-1607611; he thanks the Center for its hospitality during the neutron stars workshop in June and July 2017. NE-R acknowledges the hospitality of the 'Institut de Ciències de l'Espai (CSIC), where this work was completed.

This research is based on observations made with the Nordic Optical Telescope, operated by the Nordic Optical Telescope Scientific Association at the Observatorio del Roque de los Muchachos, La Palma, Spain, of the Instituto de Astrofísica de Canarias; the Gran Telescopio Canarias (GTC), installed in the Spanish Observatorio del Roque de los Muchachos of the Instituto de Astrofísica de Canarias, on the island of La Palma; the Italian Telescopio Nazionale Galileo (TNG), operated on the island of La Palma by the Fundaci Galileo Galilei of the INAF (Istituto Nazionale di Astrofisica) at the Spanish Observatorio del Roque de los Muchachos of the Instituto de Astrofísica de Canarias; the Liverpool Telescope, operated on the island of La Palma by Liverpool John Moores University in the Spanish Observatorio del Roque de los Muchachos of the Instituto de Astrofísica de Canarias with financial support from the UK Science and Technology Facilities Council; the 1.82-m Copernico Telescope and the Schmidt 67/92 cm of INAF-Asiago Observatory; the Catalina Real Time Survey (CRTS) Catalina Sky Survey (CSS) 0.7-m Schmidt Telescope; and the Las Cumbres Observatory (LCO) network. This work is also based in part on archival data obtained with the NASA/ESA *Hubble Space Telescope*, obtained from the Data Archive at the Space Telescope Science Institute (STScI), which is operated by the Association of Universities for Research in Astronomy (AURA), Inc., under NASA contract NAS5-26555; the *Spitzer Space Telescope*, which is operated by the Jet Propulsion Laboratory, California Institute of Technology, under a contract with NASA (support was provided by NASA through an award issued by JPL/Caltech); and the *Swift* telescope.

This work has made use of the NASA/IPAC Extragalactic Database (NED), which is operated by the Jet Propulsion Laboratory, California Institute of Technology, under contract with NASA.

REFERENCES

Anderson J. P. et al., 2014, ApJ, 786, 67
Benetti S. et al., 2016, MNRAS, 456, 3296
Bertola F., 1963, Contrib. dell'Osservatorio Astrofis. dell'Universita di Padova in Asiago, 142, 3
Bertola F., 1964, Ann. d'Astrophysique, 27, 319
Bertola F., 1965, Contrib. dell'Osservatorio Astrofis. dell'Universita di Padova in Asiago, 171, 3
Bertola F., 1967, Inf. Bull. Var. Stars, 196, 1
Cardelli J. A., Clayton G. C., Mathis J. S., 1989, ApJ, 345, 245
Chevalier R. A., Irwin C. M., 2012, ApJ, 747, L17
Chonis T. S., Gaskell C. M., 2008, AJ, 135, 264
Chugai N. N., 2001, MNRAS, 326, 1448
Dolphin A. E., 2000, PASP, 112, 1383
Drake A. J. et al., 2009, ApJ, 696, 870
Elias-Rosa N., 2007, in di Salvo T., Israel G. L., Piersant L., Burderi L., Matt G., Tornambe A., Menna M. T., eds, AIP Conf. Ser. Vol. 924, The Multicolored Landscape of Compact Objects and Their Explosive Origins. Am. Inst. Phys., New York, p. 395
Elias-Rosa N. et al., 2013, .Astron. Telegram, 5521
Elias-Rosa N. et al., 2016, MNRAS, 463, 3894
Fassia A. et al., 2000, MNRAS, 318, 1093
Foley R. J., Berger E., Fox O., Levesque E. M., Challis P. J., Ivans I. I., Rhoads J. E., Soderberg A. M., 2011, ApJ, 732, 32
Fox O. D. et al., 2011, ApJ, 741, 7
Fox O. D., Filippenko A. V., Skrutskie M. F., Silverman J. M., Ganeshalingam M., Cenko S. B., Clubb K. I., 2013, AJ, 146, 2
Fraser M. et al., 2013, MNRAS, 433, 1312
Fraser M. et al., 2015, MNRAS, 453, 3886
Fuller J., 2017, MNRAS, 470, 1642
Graham M. L. et al., 2017, MNRAS, 469, 1559
Humphreys R. M., Martin J. C., 2012, in Davidson K., Humphreys R. M., eds, Astrophysics and Space Science Library, Vol. 384, Eta Carinae and the Supernova Impostors. Springer-Verlag, Berlin, p. 1
Kankare E. et al., 2015, A&A, 581, L4
Kiewe M. et al., 2012, ApJ, 744, 10
Kochanek C. S., Szczygiel D. M., Stanek K. Z., 2011, ApJ, 737, 76
Liu Q.-Z., Hu J.-Y., Hang H.-R., Qiu Y.-L., Zhu Z.-X., Qiao Q.-Y., 2000, A&AS, 144, 219
Margutti R. et al., 2014, ApJ, 780, 21
Mauerhan J. C. et al., 2013, MNRAS, 430, 1801
Maza J. et al., 2009, Cent. Bur. Electron. Telegrams, 1928, 1
Miller A. A. et al., 2010, MNRAS, 404, 305
Mould J. R. et al., 2000, ApJ, 529, 786
Ofek E. O. et al., 2013a, Nature, 494, 65
Ofek E. O. et al., 2013b, ApJ, 763, 42
Ofek E. O. et al., 2014, ApJ, 789, 104
Ofek E. O. et al., 2016, ApJ, 824, 6
Pastorello A. et al., 2013a, ApJ, 767, 1
Pastorello A. et al., 2013b, Astron. Telegram, 5358
Pastorello A. et al., 2013c, Astron. Telegram, 5359
Pastorello A. et al., 2017, MNRAS, 474, 197
Phillips M. M. et al., 2013, ApJ, 779, 38
Poznanski D., Ganeshalingam M., Silverman J. M., Filippenko A. V., 2011, MNRAS, 415, L81

Poznanski D., Prochaska J. X., Bloom J. S., 2012, MNRAS, 426, 1465
Pozzo M., Meikle W. P. S., Fassia A., Geballe T., Lundqvist P., Chugai N. N., Sollerman J., 2004, MNRAS, 352, 457
Quataert E., Shiode J., 2012, MNRAS, 423, L92
Roming P. W. A. et al., 2012, ApJ, 751, 92
Schlafly E. F., Finkbeiner D. P., 2011, ApJ, 737, 103
Smith N., 2008, Nature, 455, 201
Smith N., 2012, in Davidson K., Humphreys R. M., eds, Astrophysics and Space Science Library, Vol. 384, Eta Carinae and the Supernova Impostors. Springer-Verlag, Berlin, p. 145
Smith N., 2014, ARA&A, 52, 487
Smith N., 2016, preprint (arXiv:1612.02006)
Smith N., Arnett W. D., 2014, ApJ, 785, 82
Smith N., Frew D. J., 2011, MNRAS, 415, 2009
Smith N. et al., 2010, AJ, 139, 1451
Smith N., Li W., Silverman J. M., Ganeshalingam M., Filippenko A. V., 2011, MNRAS, 415, 773
Smith N. et al., 2012, MNRAS, 420, 1135
Smith N., Mauerhan J. C., Prieto J. L., 2014, MNRAS, 438, 1191
Taddia F. et al., 2013, A&A, 555, A10
Tartaglia L. et al., 2016, MNRAS, 459, 1039
Terreran G. et al., 2016, MNRAS, 462, 137
Thöne C. C. et al., 2017, A&A, 599, A129
Turatto M., Benetti S., Cappellaro E., 2003, in Hillebrandt W., Leibundgut B., eds, From Twilight to Highlight: The Physics of Supernovae. Springer-Verlag, Berlin, p. 200
Van Dyk S. D., Matheson T., 2012a, in Davidson K., Humphreys R. M., eds, Astrophysics and Space Science Library, Vol. 384, Eta Carinae and the Supernova Impostors. Springer-Verlag, Berlin, p. 249
Van Dyk S. D., Matheson T., 2012b, ApJ, 746, 179
Van Dyk S. D., Peng C. Y., King J. Y., Filippenko A. V., Treffers R. R., Li W., Richmond M. W., 2000, PASP, 112, 1532

APPENDIX A: PROPERTIES OF THE SUPERNOVAE USED IN THIS WORK

Table A1. Properties of the transients used in this work.

Object	Host galaxy	Redshift	Distance† (Mpc)	$E(B-V)_{\rm tot}$ (mag)	V max date (MJD)	Sources
SN 1961V	NGC 1058	0.002	9.3	0.05	37641.0	a
η Car	–	0.00008	0.0023	0.24	~ -5000.0	b
SN 1996al	NGC 7689	0.007	22.9	0.11	50265.0	c
SN 2009ip	NGC 7259	0.006	25.0	0.02	56207.7	d
SN 2015bh	NGC 2770	0.007	29.3	0.21	57166.9	e
SNhunt248	NGC 5806	0.005	21.9	0.05	56828.0‡	f
SNhunt151	UGC 3165	0.013	51.8	0.64	56571.8	This work

†Distances have been scaled to $H_0 = 73\,{\rm km\,s^{-1}\,Mpc^{-1}}$.
‡This epoch corresponds to the '2014b' peak of SNhunt248.
a = Bertola 1963, 1964, 1965, 1967; b = Smith & Frew 2011; Humphreys & Martin 2012; c = Benetti et al. 2016; d = Maza et al. 2009; Smith et al. 2010; Foley et al. 2011; Pastorello et al. 2013a; Mauerhan et al. 2013; Fraser et al. 2013; e = Elias-Rosa et al. 2016; f=Kankare et al. 2015.

APPENDIX B: TABLES OF PHOTOMETRY AND SPECTROSCOPY OF SNHUNT151

Table B1. Basic information about the telescopes and instruments used (in alphabetical key order).

Tables Code	Telescope	Instrument	Pixel scale (arcsec pixel^{-1})	Location
AFOSC	1.82 m Copernico Telescope	AFOSC	0.52	Mount Ekar, Asiago, Italy
ALFOSC	2.56 m Nordic Optical Telescope	ALFOSC	0.19	Roque de Los Muchachos, La Palma, Canary Islands, Spain
Apogee	0.53 m Ritchey-Chretien Telescope	Apogee	1.17	Osservatorio Astronomico Provinciale di Montarrenti, Siena, Italy
FLI-New	0.50 m Newtonian Telescope	FLI Proline CCD	2.32	Osservatorio di Monte Agliale,Lucca, Italy
IO:O	2.00 m Liverpool Telescope	IO:O	0.30	Roque de Los Muchachos, La Palma, Canary Islands, Spain
kb71	1.00 m-03 Telescope	kb71	0.47	LCOGT[a] node at Siding Spring Observatory, Australia
kb77	1.00 m-04 Telescope	kb77	0.47	LCOGT node at Cerro Tololo Inter-American Observatory, Chile
kb78	1.00 m-05 Telescope	kb78	0.47	LCOGT node at Cerro Tololo Inter-American Observatory, Chile
kb74	1.00 m-08 Telescope	kb74	0.47	LCOGT node at Cerro Tololo Inter-American Observatory, Chile
kb73	1.00 m-09 Telescope	kb73	0.47	LCOGT node at Cerro Tololo Inter-American Observatory, Chile
kb70	1.00 m-10 Telescope	kb70	0.47	LCOGT node at South African Astronomical Observatory, South African
kb05	1.00 m-11 Telescope	kb05	0.47	LCOGT node at Siding Spring Observatory, Australia
kb75	1.00 m-12 Telescope	kb75	0.47	LCOGT node at South African Astronomical Observatory, South African
kb79	1.00 m-13 Telescope	kb79	0.47	LCOGT node at South African Astronomical Observatory, South African
kb76	1.00 m-13 Telescope	kb76	0.47	LCOGT node at South African Astronomical Observatory, South African
LRS	3.58 m Telescopio Nazionale Galileo	LRS	0.25	Roque de Los Muchachos, La Palma, Canary Islands, Spain
NOTCam	2.56 m Nordic Optical Telescope	NOTCam	0.24	Roque de Los Muchachos, La Palma, Canary Islands, Spain
NICS	3.58 m Telescopio Nazionale Galileo	NICS	0.25	Roque de Los Muchachos, La Palma, Canary Islands, Spain
OSIRIS	10.4 m Gran Telescopio CANARIAS	OSIRIS	0.25	Roque de Los Muchachos, La Palma, Canary Islands, Spain
Palomar	5.10 m Hale Telescope	DBSP	0.39	Palomar Observatory, California, USA
PTF	1.20 m Samuel Oschin Telescope	CCD	1.01	Palomar Observatory, California, USA
RATCam	2.00 m Liverpool Telescope	RATCam	0.28	Roque de Los Muchachos, La Palma, Canary Islands, Spain
SBIG	0.67/0.92 m Schmidt Telescope	SBIG	0.86	Mount Ekar, Asiago, Italy
SDSS	2.50 m Telescope	Sloan Digital Sky Survey CCD	0.39	Apache Point Observatory, New Mexico, USA
SI	1.52 m Cassegrain reflector	SI 600-386	0.96	Catalina Sky Survey node at Mount Lemmon Observatory, USA
SOAR	4.10 m Southern Astrophysical Research Telescope	Goodman	0.15	Cerro Tololo Inter-American Observatory, Chile
Spitzer	0.8-m Spitzer Space Telescipe	IRAC	0.60	–
T17FLI	0.43 m iTelescope.Net T17	FLI-New-Beta	0.92	Siding Spring Observatory, Australia
T18SBIG	0.32 m iTelescope.Net T18	SBIG STL-6303 3 CCD Camera	0.63	AstroCamp Observatory, Nerpio, Spain
T21FLI	0.43 m iTelescope.Net T21	FLI-New	0.96	Mayhill, New Mexico, USA
T7SBIG	0.43 m iTelescope.Net T7	SBIG STL-11000 3 CCD Camera	0.73	AstroCamp Observatory, Nerpio, Spain
T9SBIG	0.32 m iTelescope.Net T9	SBIG ST-8 3 CCD Camera	0.80	AstroCamp Observatory, Nerpio, Spain
WFC3	2.40 m Hubble Space Telescope	WFC3/UVIS	0.04	–

[a] LCOGT = Las Cumbres Observatory Global Telescope Network.

Table B2. Optical Johnson–Cousins photometry of SNhunt151 (VEGAMAG).

Date	MJD	Phase[a] (days)	*B* (mag)	*V* (mag)	*R* (mag)	*I* (mag)	Instrument key
20051028	53671.48	−2900.4	–	>22.5	–	–	SI
20051227	53731.40	−2840.4	–	>21.8	–	–	SI
20060125	53760.44	−2811.4	–	>21.4	–	–	SI
20060126	53761.23	−2810.6	–	>21.4	–	–	SI
20060202	53768.29	−2803.6	–	>22.1	–	–	SI
20060303	53797.32	−2774.5	–	>21.6	–	–	SI
20060928	54006.43	−2565.4	–	>21.6	–	–	SI
20061020	54028.43	−2543.4	–	>22.0	–	–	SI
20061101	54040.31	−2531.5	–	>21.8	–	–	SI
20061217	54086.26	−2485.6	–	>21.6	–	–	SI
20070207	54138.18	−2433.7	–	>22.4	–	–	SI
20070313	54172.18	−2399.7	–	>21.7	–	–	SI
20071016	54389.42	−2182.4	–	>21.6	–	–	SI
20071215	54449.38	−2122.5	–	>21.8	–	–	SI
20071231	54465.20	−2106.7	–	>21.9	–	–	SI
20080112	54477.29	−2094.6	–	>21.7	–	–	SI
20080207	54503.15	−2068.7	–	>21.6	–	–	SI
20080312	54537.12	−2034.7	–	>21.7	–	–	SI
20080404	54560.13	−2011.7	–	>21.7	–	–	SI
20080928	54737.45	−1834.4	–	>21.7	–	–	SI
20081130	54800.39	−1771.5	–	>21.6	–	–	SI
20090120	54851.20	−1720.7	–	>21.4	–	–	SI
20091017	55121.47	−1450.4	–	>22.2	–	–	SI
20091109	55144.44	−1427.4	–	>21.4	–	–	SI
20091111	55146.98	−1424.9	–	–	>20.0	–	Apogee
20091210	55175.20	−1396.7	–	>21.6	–	–	SI
20100107	55203.22	−1368.6	–	>21.7	–	–	SI
20100220	55247.12	−1324.7	–	>21.6	–	–	SI
20100319	55274.15	−1297.7	–	>21.8	–	–	SI
20100906	55445.37	−1126.5	–	–	>20.6	–	PTF
20101020	55489.99	−1081.9	–	–	>19.2	–	Apogee
20101128	55528.31	−1043.5	–	>21.5	–	–	SI
20101203	55533.33	−1038.5	–	>21.9	–	–	SI
20101209	55539.98	−1031.9	–	–	>19.5	–	Apogee
20101225	55555.26	−1016.6	–	>21.9	–	–	SI
20110112	55573.08	−998.8	–	>21.6	–	–	SI
20110127	55588.16	−983.7	–	>21.9	–	–	SI
20110207	55599.21	−972.6	–	–	>20.5	–	PTF
20110306	55626.12	−945.7	–	>21.6	–	–	SI
20110326	55646.14	−925.7	–	>21.1	–	–	SI
20111031	55865.11	−706.7	–	–	>19.4	–	Apogee
20111117	55882.05	−689.8	–	–	>19.1	–	Apogee
20111225	55920.18	−651.7	–	21.75 (0.35)	–	–	SI
20120117	55943.80	−628.0	–	–	>19.2	–	Apogee
20120129	55955.13	−616.7	–	21.68 (0.30)	–	–	SI
20120217	55974.82	−597.0	–	–	>19.4	–	Apogee
20120226	55983.79	−588.1	–	–	>19.4	–	Apogee
20120314	56000.16	−571.7	–	21.79 (0.40)	–	–	SI
20120323	56009.17	−562.7	–	21.69 (0.47)	–	–	SI
20120925	56195.41	−376.4	–	20.86 (0.21)	–	–	SI
20120926	56196.42	−375.4	–	20.81 (0.43)	–	–	T21FLI
20121023	56223.10	−348.8	–	–	19.57 (0.46)	–	Apogee
20121107	56238.34	−333.5	–	20.71 (0.19)	–	–	SI
20121203	56264.18	−307.7	–	20.64 (0.48)	–	–	SI
20121208	56269.31	−302.5	–	20.59 (0.19)	–	–	SI
20121211	56272.98	−298.9	–	–	19.33 (0.22)	–	Apogee
20130106	56298.22	−273.6	–	20.60 (0.20)	–	–	SI
20130107	56303.91	−267.9	–	–	>18.7	–	Apogee
20130113	56305.17	−266.7	–	20.55 (0.21)	–	–	SI
20130203	56326.74	−245.1	–	–	19.21 (0.19)	–	Apogee
20130223	56346.19	−225.7	–	20.50 (0.24)	–	–	SI
20130818	56522.14	−49.7	–	–	17.93 (0.33)	–	FLI-New
20130819	56523.11	−48.7	–	–	17.91 (0.28)	–	FLI-New

Table B2 *– continued*

Date	MJD	Phase[a] (days)	*B* (mag)	*V* (mag)	*R* (mag)	*I* (mag)	Instrument key
20130820	56524.17	−47.7	–	–	17.87 (0.24)	–	LRS
20130821	56525.06	−46.8	19.39 (0.24)	18.54 (0.13)	17.72 (0.09)	17.40 (0.09)	SBIG
20130821	56525.43	−46.4	19.35 (0.12)	18.41 (0.07)	–	–	kb74
20130822	56526.10	−45.8	19.31 (0.24)	18.50 (0.20)	17.67 (0.11)	17.31 (0.09)	SBIG
20130822	56526.44	−45.4	19.34 (0.11)	18.40 (0.05)	–	–	kb74
20130824	56528.79	−43.1	19.25 (0.17)	18.50 (0.08)	–	–	kb71
20130825	56529.40	−42.4	19.22 (0.09)	18.41 (0.06)	–	–	kb78
20130828	56532.39	−39.5	19.02 (0.08)	18.30 (0.04)	–	–	kb73
20130901	56536.08	−35.8	18.87 (0.12)	18.08 (0.06)	17.29 (0.08)	16.93 (0.12)	AFOSC
20130905	56540.16	−31.7	–	–	17.39 (0.20)	–	Apogee
20130905	56540.39	−31.5	–	18.04 (0.19)	–	–	T21FLI
20130906	56541.46	−30.4	18.89 (0.05)	18.06 (0.04)	–	–	kb74
20130907	56542.44	−29.4	18.83 (0.06)	17.99 (0.04)	–	–	kb74
20130913	56548.18	−23.7	18.68 (0.04)	17.93 (0.03)	–	–	IO:O
20130913	56548.43	−23.4	18.69 (0.05)	17.88 (0.04)	–	–	kb74
20130914	56549.43	−22.4	18.62 (0.04)	17.82 (0.03)	–	–	kb74
20130922	56557.12	−14.7	–	–	16.94 (0.18)	–	Apogee
20130924	56559.08	−12.8	18.35 (0.03)	17.56 (0.04)	–	–	kb70
20130925	56560.39	−11.5	18.32 (0.06)	17.52 (0.04)	–	–	kb74
20130926	56561.39	−10.5	18.27 (0.05)	17.52 (0.04)	–	–	kb74
20130928	56563.33	−8.5	18.28 (0.04)	17.49 (0.04)	–	–	kb78
20131001	56566.20	−5.7	18.22 (0.06)	17.47 (0.04)	–	–	IO:O
20131006	56571.21	−0.6	18.23 (0.03)	17.46 (0.04)	–	–	IO:O
20131007	56572.29	0.4	18.22 (0.04)	17.45 (0.04)	–	–	kb73
20131008	56573.46	1.6	–	17.43 (0.22)	–	–	T21FLI
20131009	56574.06	2.2	18.22 (0.05)	17.46 (0.05)	–	–	kb70
20131010	56575.15	3.3	–	17.41 (0.24)	–	–	T18SBIG
20131011	56576.77	4.9	–	–	16.90 (0.18)	–	T17FLI
20131012	56577.35	5.5	18.23 (0.05)	17.43 (0.02)	–	–	kb78
20131014	56579.03	7.2	18.24 (0.04)	17.44 (0.04)	–	–	kb70
20131014	56579.10	7.2	–	17.49 (0.18)	–	–	T18SBIG
20131017	56582.04	10.2	18.33 (0.06)	17.53 (0.04)	–	–	kb75
20131017	56582.44	10.6	–	17.51 (0.18)	–	–	T21FLI
20131019	56584.68	12.8	–	–	16.98 (0.21)	–	T17FLI
20131020	56585.04	13.2	18.36 (0.05)	17.56 (0.04)	–	–	kb70
20131024	56589.68	17.8	–	–	17.10 (0.31)	–	T17FLI
20131026	56591.35	19.5	18.61 (0.05)	17.80 (0.05)	–	–	kb73
20131026	56591.63	19.8	–	17.86 (0.24)	–	–	T9SBIG
20131026	56591.67	19.8	–	–	17.09 (0.16)	–	T17FLI
20131028	56593.09	21.2	–	17.77 (0.13)	–	–	T18SBIG
20131028	56593.38	21.5	–	17.83 (0.08)	17.06 (0.05)	–	T21FLI
20131030	56595.04	23.2	–	–	17.26 (0.16)	–	T17FLI
20131030	56595.21	23.4	18.68 (0.04)	17.89 (0.04)	–	–	IO:O
20131101	56597.08	25.2	–	–	17.14 (0.18)	–	Apogee
20131102	56598.50	26.7	18.86 (0.05)	17.99 (0.04)	–	–	kb74
20131104	56600.99	29.1	18.89 (0.06)	18.01 (0.05)	–	–	kb75
20131104	56601.00	29.1	18.84 (0.05)	18.04 (0.04)	–	–	kb75
20131105	56601.10	29.2	18.86 (0.04)	18.04 (0.04)	–	–	IO:O
20131107	56603.04	31.2	18.91 (0.04)	18.05 (0.02)	–	–	IO:O
20131107	56603.10	31.2	18.84 (0.07)	18.10 (0.05)	17.20 (0.07)	16.80 (0.04)	SBIG
20131107	56603.42	31.6	–	18.03 (0.16)	–	–	T21FLI
20131108	56604.24	32.4	18.93 (0.05)	18.06 (0.03)	–	–	kb78
20131111	56607.25	35.4	19.01 (0.06)	18.17 (0.04)	–	–	kb77
20131111	56607.28	35.4	19.04 (0.06)	18.18 (0.04)	–	–	kb78
20131112	56608.12	36.3	–	18.15 (0.21)	–	–	T18SBIG
20131112	56608.89	37.0	18.92 (0.07)	18.25 (0.07)	17.26 (0.07)	16.89 (0.07)	SBIG
20131113	56609.01	37.2	–	18.17 (0.08)	17.28 (0.07)	–	T7SBIG
20131115	56611.08	39.2	19.06 (0.06)	18.25 (0.04)	–	–	IO:O
20131115	56611.19	39.3	19.11 (0.08)	18.22 (0.04)	–	–	kb78
20131117	56613.25	41.4	19.25 (0.13)	18.32 (0.06)	–	–	kb78
20131120	56616.29	44.4	19.22 (0.11)	18.49 (0.08)	–	–	kb78
20131122	56618.05	46.2	19.36 (0.04)	18.49 (0.03)	–	–	IO:O
20131122	56618.96	47.1	19.35 (0.07)	18.57 (0.06)	–	–	kb79

Table B2 – *continued*

Date	MJD	Phase[a] (days)	*B* (mag)	*V* (mag)	*R* (mag)	*I* (mag)	Instrument key
20131124	56620.98	49.1	19.41 (0.04)	18.57 (0.03)	–	–	IO:O
20131126	56622.04	50.2	–	–	17.66 (0.21)	–	Apogee
20131126	56622.99	51.1	19.48 (0.04)	18.61 (0.04)	–	–	IO:O
20131127	56623.14	51.3	19.55 (0.07)	18.60 (0.06)	–	–	kb78
20131129	56625.04	53.2	19.50 (0.04)	18.64 (0.03)	–	–	IO:O
20131129	56625.18	53.3	19.59 (0.05)	18.63 (0.04)	–	–	kb78
20131202	56628.54	56.7	19.57 (0.07)	18.74 (0.04)	–	–	kb05
20131202	56628.96	57.1	–	18.70 (0.13)	17.84 (0.10)	–	T7SBIG
20131203	56629.95	58.1	–	–	17.99 (0.25)	–	Apogee
20131206	56632.00	60.2	–	–	–	17.59 (0.21)	AFOSC
20131207	56633.00	61.2	–	18.81 (0.20)	–	–	T7SBIG
20131208	56634.14	62.3	19.77 (0.07)	18.86 (0.05)	–	–	kb74
20131208	56634.97	63.1	–	–	18.00 (0.24)	–	Apogee
20131210	56636.32	64.5	19.86 (0.06)	18.89 (0.05)	–	–	kb74
20131214	56640.33	68.5	19.99 (0.16)	18.99 (0.13)	–	–	kb74
20131217	56643.97	72.1	–	–	18.36 (0.30)	–	Apogee
20131222	56648.47	76.6	20.13 (0.18)	19.16 (0.07)	–	–	kb71
20131223	56649.76	77.9	–	19.25 (0.26)	18.31 (0.12)	–	T7SBIG
20131225	56651.92	80.1	20.21 (0.13)	19.22 (0.05)	–	–	kb75
20140101	56658.93	87.1	–	–	18.66 (0.20)	–	Apogee
20140102	56659.97	88.1	20.38 (0.07)	19.36 (0.04)	–	–	IO:O
20140103	56660.96	89.1	20.42 (0.04)	19.43 (0.04)	18.50 (0.03)	18.11 (0.05)	LRS
20140104	56661.96	90.1	20.45 (0.04)	19.40 (0.03)	–	–	IO:O
20140106	56663.91	92.1	–	–	18.79 (0.37)	–	Apogee
20140107	56664.89	93.0	20.54 (0.36)	19.58 (0.09)	18.59 (0.04)	18.26 (0.09)	AFOSC
20140107	56664.93	93.1	20.55 (0.32)	19.52 (0.09)	–	–	IO:O
20140117	56674.33	102.5	20.61 (0.30)	19.78 (0.28)	–	–	kb74
20140121	56678.84	107.0	20.73 (0.23)	19.78 (0.13)	18.89 (0.47)	18.42 (0.17)	SBIG
20140125	56682.74	110.9	20.75 (0.23)	19.86 (0.10)	18.95 (0.05)	18.68 (0.15)	AFOSC
20140126	56683.76	111.9	–	–	19.11 (0.31)	–	Apogee
20140128	56685.45	113.6	20.99 (0.25)	19.84 (0.07)	–	–	kb71
20140128	56685.92	114.1	20.89 (0.09)	19.98 (0.07)	–	–	IO:O
20140131	56688.44	116.6	21.18 (0.32)	20.02 (0.09)	–	–	kb71
20140202	56690.80	119.0	20.95 (0.42)	20.20 (0.10)	–	–	kb70
20140205	56693.91	122.1	21.14 (0.10)	20.18 (0.05)	–	–	IO:O
20140206	56694.72	122.9	–	–	19.14 (0.45)	–	Apogee
20140207	56695.43	123.6	21.05 (0.33)	20.35 (0.14)	–	–	kb05
20140208	56696.44	124.6	–	20.20 (0.33)	–	–	kb71
20140211	56699.86	128.0	21.14 (0.10)	20.25 (0.09)	–	–	IO:O
20140214	56702.86	131.0	20.98 (0.25)	20.25 (0.20)	–	–	IO:O
20140301	56717.86	146.0	21.79 (0.08)	20.52 (0.05)	19.55 (0.05)	19.07 (0.04)	LRS
20140302	56718.77	146.9	–	–	19.39 (0.28)	–	Apogee
20140330	56746.85	175.0	–	21.02 (0.43)	20.34 (0.33)	19.73 (0.33)	AFOSC
20140330	56746.85	175.0	>19.5	–	–	–	AFOSC
20140805	56874.21	302.4	23.38 (0.17)	21.96 (0.07)	21.03 (0.09)	20.83 (0.09)	ALFOSC
20140825	56894.20	322.3	23.24 (0.11)	22.12 (0.08)	21.14 (0.06)	21.01 (0.09)	ALFOSC
20140918	56918.20	346.3	23.36 (0.14)	22.34 (0.10)	21.37 (0.12)	21.16 (0.15)	ALFOSC
20141013	56943.21	371.4	23.33 (0.27)	22.55 (0.19)	21.67 (0.20)	21.23 (0.25)	ALFOSC
20141027	56957.27	385.4	23.54 (0.14)	22.62 (0.07)	21.64 (0.10)	21.27 (0.18)	ALFOSC
20141112	56973.20	401.4	23.38 (0.20)	22.76 (0.13)	21.64 (0.14)	21.09 (0.14)	ALFOSC
20141124	56986.01	414.2	23.63 (0.12)	22.63 (0.08)	21.65 (0.11)	21.21 (0.13)	ALFOSC
20150124	57046.87	475.0	–	–	22.02 (0.24)	–	ALFOSC
20150310	57091.94	520.1	–	–	22.11 (0.19)	–	ALFOSC
20150806	57240.20	668.3	–	–	>21.2	–	ALFOSC
20161023	57684.97	1113.1	–	23.24 (0.02)	–	21.95 (0.01)	WFC3

[a] Phases are relative to *V* maximum light, MJD = 56571.8 ± 1.0.

Table B3. Optical Sloan photometry of SNhunt151 (ABMAG).

Date	MJD	Phase[a] (days)	*u* (mag)	*g* (mag)	*r* (mag)	*i* (mag)	*z* (mag)	Instrument key
20031221	52994.50	−3577.4	>22.5	>22.8	>22.3	>22.1	>21.6	SDSS
20110207	55599.14	−972.7	–	>21.5	–	–	–	PTF
20110208	55600.13	−971.7	–	>21.0	–	–	–	PTF
20130821	56525.44	−46.4	–	18.96 (0.06)	17.93 (0.05)	17.66 (0.04)	–	kb74
20130822	56526.45	−45.4	–	18.95 (0.04)	17.87 (0.04)	17.64 (0.04)	–	kb74
20130824	56528.80	−43.0	–	18.95 (0.08)	17.82 (0.05)	17.64 (0.04)	–	kb71
20130825	56529.42	−42.4	–	18.88 (0.05)	17.81 (0.04)	17.60 (0.04)	–	kb78
20130828	56532.42	−39.4	–	–	17.68 (0.04)	17.43 (0.02)	–	kb73
20130830	56534.17	−37.7	–	–	17.62 (0.03)	17.42 (0.02)	–	RATCam
20130906	56541.47	−30.4	–	18.45 (0.03)	17.50 (0.04)	17.29 (0.04)	–	kb74
20130907	56542.46	−29.4	–	18.46 (0.05)	17.43 (0.04)	17.27 (0.04)	–	kb74
20130913	56548.18	−23.7	19.29 (0.06)	–	17.42 (0.03)	17.26 (0.02)	–	IO:O
20130914	56549.46	−22.4	–	18.17 (0.03)	17.28 (0.02)	17.05 (0.02)	–	kb74
20130924	56559.10	−12.8	–	17.93 (0.04)	17.00 (0.03)	16.78 (0.03)	–	kb70
20130925	56560.42	−11.4	–	17.86 (0.03)	16.95 (0.04)	16.72 (0.03)	–	kb74
20130926	56561.42	−10.4	–	17.89 (0.02)	16.98 (0.03)	16.74 (0.02)	–	kb74
20130928	56563.36	−8.5	–	17.91 (0.02)	16.93 (0.03)	16.68 (0.02)	–	kb78
20131001	56566.20	−5.7	18.78 (0.11)	–	16.90 (0.03)	16.73 (0.03)	–	IO:O
20131006	56571.21	−0.6	18.83 (0.05)	17.84 (0.02)	16.87 (0.03)	16.72 (0.02)	–	IO:O
20131007	56572.30	0.5	–	17.81 (0.05)	16.86 (0.04)	16.67 (0.04)	–	kb73
20131009	56574.07	2.2	–	17.79 (0.03)	16.87 (0.03)	16.68 (0.03)	–	kb70
20131012	56577.36	5.5	–	17.79 (0.02)	16.86 (0.03)	16.64 (0.02)	–	kb78
20131014	56579.04	7.2	–	17.84 (0.03)	16.91 (0.03)	16.66 (0.03)	–	kb70
20131017	56582.05	10.2	–	17.90 (0.03)	16.95 (0.02)	16.70 (0.03)	–	kb75
20131020	56585.07	13.2	–	17.91 (0.12)	–	16.76 (0.16)	–	kb70
20131026	56591.32	19.5	–	18.18 (0.04)	17.19 (0.02)	16.97 (0.02)	16.79 (0.06)	kb73
20131030	56595.21	23.4	19.49 (0.12)	18.31 (0.03)	17.22 (0.03)	17.09 (0.03)	–	IO:O
20131102	56598.68	26.8	–	18.44 (0.03)	17.29 (0.03)	17.17 (0.03)	16.90 (0.05)	kb71
20131105	56601.10	29.2	19.70 (0.10)	18.47 (0.03)	17.32 (0.02)	17.24 (0.03)	–	IO:O
20131105	56601.24	29.4	–	18.48 (0.03)	17.34 (0.05)	17.21 (0.03)	16.99 (0.05)	kb73
20131107	56603.04	31.2	19.73 (0.12)	18.52 (0.03)	17.34 (0.03)	17.27 (0.04)	–	IO:O
20131108	56604.30	32.5	–	18.56 (0.03)	17.38 (0.03)	17.24 (0.02)	17.02 (0.04)	kb78
20131111	56607.26	35.4	–	18.60 (0.02)	17.48 (0.02)	17.30 (0.04)	17.09 (0.07)	kb77
20131112	56608.43	36.6	–	18.65 (0.03)	17.48 (0.03)	17.33 (0.03)	17.12 (0.06)	kb74
20131115	56611.08	39.2	20.12 (0.15)	18.64 (0.04)	17.53 (0.03)	17.46 (0.03)	–	IO:O
20131116	56612.25	40.4	–	18.75 (0.03)	17.55 (0.03)	17.45 (0.02)	–	kb77
20131117	56613.21	41.4	–	18.67 (0.12)	–	17.52 (0.22)	17.29 (0.10)	kb77
20131120	56616.22	44.4	–	18.82 (0.08)	17.67 (0.04)	17.57 (0.05)	17.34 (0.08)	kb73
20131122	56618.04	46.2	20.39 (0.09)	18.93 (0.02)	17.73 (0.02)	17.70 (0.02)	–	IO:O
20131123	56619.16	47.3	–	18.96 (0.04)	17.69 (0.03)	17.76 (0.04)	17.46 (0.05)	kb73
20131124	56620.97	49.1	20.45 (0.06)	18.95 (0.03)	17.76 (0.03)	17.75 (0.03)	–	IO:O
20131126	56622.23	50.4	–	19.02 (0.04)	17.80 (0.04)	17.77 (0.03)	17.59 (0.06)	kb77
20131126	56622.99	51.1	20.52 (0.10)	19.07 (0.03)	17.81 (0.02)	17.76 (0.03)	–	IO:O
20131129	56625.04	53.2	20.56 (0.06)	19.11 (0.03)	17.86 (0.03)	17.83 (0.03)	–	IO:O
20131130	56626.20	54.3	–	19.13 (0.03)	17.86 (0.03)	17.80 (0.02)	17.67 (0.06)	kb78
20131202	56628.56	56.7	–	19.23 (0.04)	17.95 (0.03)	17.86 (0.04)	17.73 (0.10)	kb05
20131214	56640.15	68.3	–	19.54 (0.09)	18.30 (0.05)	18.22 (0.04)	18.04 (0.09)	kb77
20131222	56648.08	76.2	–	19.71 (0.04)	18.41 (0.04)	18.36 (0.04)	–	kb77
20131225	56651.88	80.0	–	19.76 (0.03)	18.46 (0.04)	18.41 (0.04)	–	kb75
20140102	56659.96	88.1	21.47 (0.18)	19.94 (0.03)	18.54 (0.03)	18.56 (0.04)	–	IO:O
20140104	56661.96	90.1	21.54 (0.15)	19.99 (0.03)	18.58 (0.02)	18.59 (0.02)	–	IO:O
20140107	56664.93	93.1	–	20.04 (0.06)	18.63 (0.03)	18.67 (0.04)	–	IO:O
20140116	56673.34	101.5	–	20.29 (0.33)	18.70 (0.10)	18.77 (0.17)	–	kb74
20140121	56678.85	107.0	–	–	18.97 (0.04)	18.89 (0.04)	–	kb70
20140128	56685.43	113.6	–	–	19.06 (0.04)	19.05 (0.05)	–	kb71
20140128	56685.92	114.1	21.89 (0.34)	20.54 (0.07)	19.11 (0.06)	19.08 (0.16)	–	IO:O
20140204	56692.81	121.0	–	–	19.20 (0.09)	19.27 (0.20)	–	kb76
20140205	56693.91	122.1	22.25 (0.35)	20.78 (0.06)	19.23 (0.03)	19.28 (0.03)	–	IO:O
20140207	56695.45	123.6	–	–	19.24 (0.07)	19.31 (0.07)	–	kb71
20140208	56696.42	124.6	–	–	19.28 (0.10)	19.38 (0.19)	–	kb05
20140211	56699.86	128.0	–	20.83 (0.07)	19.36 (0.04)	19.42 (0.07)	–	IO:O
20140214	56702.86	131.0	–	20.75 (0.19)	19.38 (0.07)	19.44 (0.08)	–	IO:O
20140215	56703.21	131.4	–	–	19.42 (0.22)	19.27 (0.32)	–	kb74

Table B3 – *continued*

Date	MJD	Phase[a] (days)	*u* (mag)	*g* (mag)	*r* (mag)	*i* (mag)	*z* (mag)	Instrument key
20140301	56717.86	146.0	–	21.21 (0.04)	19.71 (0.03)	19.69 (0.06)	–	LRS
20140821	56890.19	318.3	–	–	21.59 (0.17)	–	–	OSIRIS
20140824	56893.21	321.4	–	22.66 (0.06)	21.37 (0.11)	21.12 (0.11)	–	OSIRIS
20141115	56976.15	404.3	–	23.03 (0.25)	–	–	–	OSIRIS
20141124	56985.21	413.4	–	>22.2	22.39 (0.22)	22.33 (0.44)	–	OSIRIS
20161207	57729.02	1157.2	–	–	>22.2	–	–	AFOSC
20170123	57776.91	1205.1	–	–	>21.6	–	–	AFOSC
20170216	57800.96	1229.1	–	24.36 (0.19)	23.26 (0.10)	23.17 (0.12)	–	OSIRIS

[a]Phases are relative to *V* maximum light, MJD = 56571.8 ± 1.0.

Table B4. NIR photometry of SNhunt151 (VEGAMAG).

Date	MJD	Phase[a] (days)	*J* (mag)	*H* (mag)	*K* (mag)	Instrument key
20131105	56600.08	28.2	15.77 (0.28)	15.48 (0.20)	15.16 (0.28)	NICS
20131119	56614.06	42.2	16.09 (0.26)	15.81 (0.26)	15.24 (0.28)	NICS
20131125	56621.04	49.2	16.18 (0.27)	16.00 (0.19)	15.39 (0.31)	NOTCam
20131127	56622.15	50.3	16.24 (0.14)	16.02 (0.22)	15.45 (0.31)	NICS
20131217	56643.07	71.2	16.85 (0.38)	16.44 (0.22)	15.94 (0.56)	NOTCam
20131223	56648.97	77.1	16.96 (0.32)	16.59 (0.26)	16.09 (0.27)	NICS
20140116	56673.94	102.1	–	–	16.66 (0.23)	NOTCam
20140212	56700.93	129.1	17.85 (0.29)	17.47 (0.27)	17.07 (0.28)	NOTCam
20140314	56730.87	159.0	18.24 (0.17)	17.98 (0.20)	17.35 (0.23)	NOTCam

[a]Phases are relative to *V* maximum light, MJD = 56571.8 ± 1.0.

Table B5. Log of spectroscopic observations of SNhunt151.

Date	MJD	Phase[a]	Instrumental setup	Grism/grating+slit	Spectral range (Å)	Resolution (Å)
20130820	56524.20	−47.6	TNG+LRS	LR-B+1.00 arcsec	3750–7850	12
20130902	56537.18	−34.7	TNG+LRS	LR-B+1.00 arcsec	3750–7850	12
20130914	56549.01	−22.8	Ekar1.82m+AFOSC	gm4+VPH6+1.69 arcsec	3800–8500	13.5/15
20131010	56575.07	3.2	TNG+LRS	LR-B+1.00 arcsec	3750–7800	12
20131019	56584.31	12.5	SOAR+Goodman	KOSI 600+0.84 arcsec	6300–8650	5
20131102	56598.05	26.2	GTC+OSIRIS	R1000B+1.00 arcsec	3600–7750	7
20131107	56603.26	31.4	GTC+OSIRIS	R1000B+1.00 arcsec	3600–7750	7
20131109	56605.39	33.5	Palomar+DBSP	BLUE (600/4000)+1.00 arcsec	4000–10000	3
20131112	56608.04	36.2	NOT+ALFOSC	gm4+1.00 arcsec	3700–8880	14
20131205	56631.06	59.2	Ekar1.82m+AFOSC	gm4+VPH6+1.69 arcsec	3900–8800	14
20131211	56637.00	65.2	Ekar1.82m+AFOSC	gm4+VPH6+1.69 arcsec	3900–8800	13.5/15
20131227	56653.75	82.0	Ekar1.82m+AFOSC	gm4+VPH6+1.69 arcsec	3900–8800	13.5/15
20140103	56660.77	89.0	TNG+LRS	LR-B/R+1.00 arcsec	3800–9150	10.5
20140301	56717.78	146.0	TNG+LRS	LR-B+1.00 arcsec	3900–8000	10.5
20140821	56890.19	318.3	GTC+OSIRIS	R1000B+1.00 arcsec	3850–7750	7
20141114	56976.16	404.3	GTC+OSIRIS	R1000B+1.00 arcsec	3850–7750	7
20131105	56601.03	29.2	TNG+NICS	IJ+1.50 arcsec	8750–13,500	28
20131118	56615.00	43.1	TNG+NICS	IJ+1.50 arcsec	8750–13,500	28
20131224	56650.84	79.0	TNG+NICS	IJ+1.50 arcsec	8700–14,500	28
20131225	56651.89	80.0	TNG+NICS	HK+1.50 arcsec	14,750–24,800	54

[a]Phases are relative to *V* maximum light, MJD = 56571.8 ± 1.0.

This paper has been typeset from a TEX/LATEX file prepared by the author.